THE MORPHOLOGY-DENSITY RELATION OF GALAXIES AT REDSHIFT 1.6

Westley Brown

A THESIS SUBMITTED TO
THE FACULTY OF GRADUATE STUDIES
IN PARTIAL FULFILLMENT OF THE REQUIREMENTS
FOR THE DEGREE OF

MASTER OF SCIENCE

Graduate Program in Physics and Astronomy
York University, Toronto, Ontario

April 2024

Abstract

We study the morphology-density relation at $z \sim 1.6$ using a sample of galaxies from three clusters and two fields. We reduce previously-obtained G102 grism spectra to obtain grism redshift estimates for galaxies in each of our clusters. Cluster and field members are selected based on their best redshift estimate, using the spectroscopic or grism redshift where available and the photometric redshift estimate otherwise. We fit F160W images of each galaxy to a single-component Sérsic profile, and define quantitative morphology classifications such that disk-like galaxies have a Sérsic index of $n < 1.5$, bulge-like galaxies have $n > 2.5$, and intermediate galaxies fall in-between. Projected local densities are calculated using 5th-Nearest Neighbours within $\Delta v = \pm 3000$ km/s, to eliminate foreground and background interlopers from neighbour selection.

We recover a relationship between morphology and local density at $z \sim 1.6$ using single-component Sérsic fits. We find that the fraction of disk-like galaxies in clusters decreases with increasing density, while the fraction of bulge-like galaxies increases. Intermediate galaxies show the weakest dependence, increasing only marginally with local density. Through direct comparison, we find no evidence of a morphology-density relation across the majority of field galaxies. We assess the morphology-mass relation and note that cluster galaxies show a much stronger dependence on stellar mass than field galaxies. This difference suggests that environmental processes directly drive the morphology-density relation, and that these environmental processes are mass-dependent. Using UVJ diagrams, we also find that clusters have a higher fraction of red and dusty galaxies compared the field. At all densities, we find a higher fraction of disk-like galaxies at $z \sim 1.6$ compared to low-redshift spirals and late-types, while our fraction of bulge-like galaxies is roughly equivalent to low-redshift ellipticals. We conclude that the morphology-density relation is already in place by

$z \sim 1.6$ for disk-like and bulge-like galaxies in clusters.

Acknowledgements

To my supervisor, Dr. Adam Muzzin, for his unwavering support, guidance, enthusiasm, and patience. He believed in me and this project even at the times I felt lowest about myself. The past few years have not been easy, especially amid the pandemic and lockdowns, and I cannot thank him enough for his patience and support that allowed me to see this thesis through and truly see my future as a researcher.

To Dr. Jasleen Matharu, who generously provided her GALFIT code, re-reduced one of the cluster images, and mentored me through the process of learning to work with grizli. This project would not be what it is without her help and expert guidance.

To my undergraduate professors at Trent University, including Dr. Dave Patton who supervised my undergraduate astronomy research and guided me through writing and publishing my first paper. Without their encouragement, I never would have thought I could make it to graduate school.

To my friends and fellow students in our research group, including Vivian, Visal, Ghassan, Sunna, and Naadiyah, for the many discussions, commiseration, and occasional distractions that have kept me sane during these past few years. And to Dr. Leo Alcorn and Dr. Cemile Marsan, who guided me through my first GALFIT mushroom clouds, provided helpful comments and questions, and helped Adam herd all of us grad students along the way. I can't imagine doing this without you.

Finally, to my parents, who have always supported me following my dreams, even when it means they have to sit through me ranting about science they don't understand. I hope they're prepared for me to do so many more times during my PhD.

Table of Contents

List of Tables

List of Figures

Chapter 1

Introduction

1.1 The Hubble classification for morphology

Just like living beings on Earth, the appearance of galaxies—their morphologies—can vary greatly. In 1926, Edwin Hubble studied the most common visual appearances of nearby galaxies, and shaped nearly the next century of extragalactic astronomy by proposing that they could largely be categorized into two dominant populations: elliptical ("early-type") or spiral ("late-type"). Known today as the Hubble sequence, this classification scheme was later expanded into more detailed morphological categories and summarized into the well-known tuning fork diagram (Hubble & Humason 1931; Sandage 1961). As shown in Figure 1.1, the tuning fork emphasizes how common galaxy morphologies can be understood to exist on a broad scale from early-type to late-type. Within each category, finer distinctions define the more specific features within each type, such as the prominence of a central bulge, the relative spacing between spiral arms, and the presence of a stellar bar in the centers of galaxies.

Today, the Hubble sequence is commonly simplified into four main categories with distinct appearances. Elliptical galaxies are typically massive and red, with a puffy, bulge-like shape that fades from its bright inner core to its faint edges. Spiral galaxies, on the other hand, are recognized predominantly by their flat and thin outer disks, which may be blue in colour. Spirals can host a range of complex visual features, such as bright spiral arms in their disks, and thick bars or compact bulges in their center. Lenticular galaxies (also

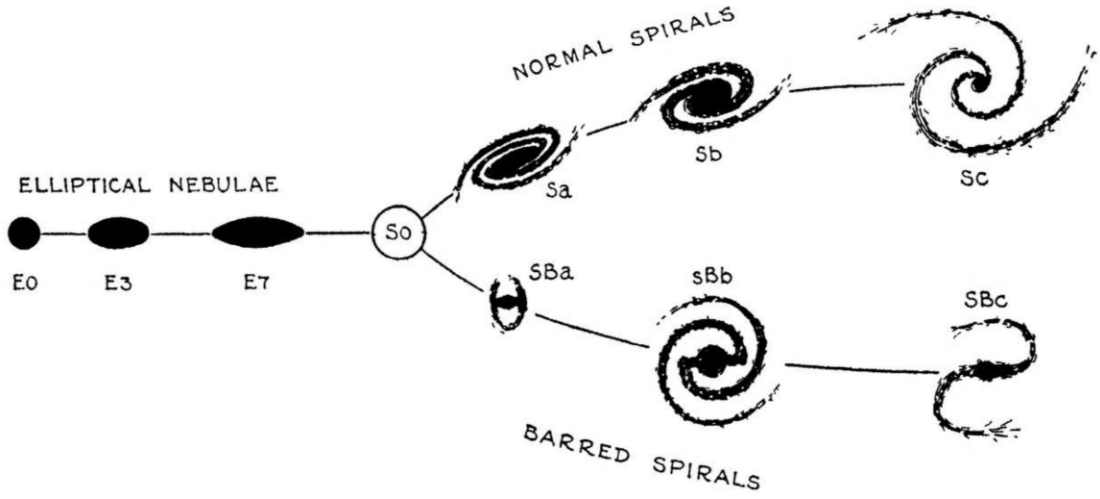

Figure 1.1: Hubble tuning fork diagram of visual galaxy morphologies, as in Hubble (1936).

known as S0s) are thought to lie somewhere between ellipticals and spirals. They typically have a large central bulge surrounded by an outer, featureless, thick disk. Irregular galaxies (also sometimes called peculiar) have uncommonly distorted and asymmetrical shapes that don't fit into the main morphological categories.

The Hubble sequence was developed purely on the visual appearance of galaxies, with no basis in theories of physical processes or galaxy evolution. Despite this, morphology has been found to correlate with many other galaxy properties, including stellar mass (Kauffmann et al. 2003), size (van der Wel et al. 2014), colour (Hubble 1936; de Vaucouleurs 1961; Strateva et al. 2001; Cassata et al. 2007), star formation rates (Brinchmann et al. 2004; Bell et al. 2012), star formation histories (Strateva et al. 2001), as well as kinematic properties such as rotational velocity (Freeman 1970), angular momentum (Harrison et al. 2017), and velocity dispersion (Djorgovski & Davis 1987). All of these aspects have become intertwined in the common understanding of galaxy classification. For example, a typical elliptical galaxy is assumed to be more massive, red, and quiescent with an older stellar population, while a typical spiral galaxy may be less massive, blue, and actively star-forming with a younger overall stellar population. These strong correlations are one reason why visual morphology is a popular method for classifying galaxies in the local universe (e.g. Dressler 1980; Bamford et al. 2009; Calvi et al. 2012).

The Hubble sequence has become so ubiquitous with the study of galaxies that astronomers even use visual classification to study galaxies in the cosmic past. In order to understand the evolution of galaxies and the universe at large, astronomers turn their attention towards galaxies at high redshift. Redshift is named for the way that wavelengths of visible light shift into the red regime as they move away from an observer, and it is a measurement that is used to refer to both a time and relative distance in space from Earth. Astronomers can measure redshift, z, directly from known spectral features, and by understanding the expansion of the universe, z can be turned into an estimate of distance and cosmological age. As redshift increases from $z = 0$, galaxies are not only farther away, but are also being observed as they were farther back in time.

Visual classification of galaxy morphologies has been used in intermediate redshift studies, within $z < 1$ (e.g. Dressler et al. 1997; Fasano et al. 2000; Poggianti et al. 2008, 2009; Just et al. 2010), as well as high redshift galaxy studies, at $z \gtrsim 1$ or more than 7.7 Gyr in the past (e.g. Postman et al. 2005; Mei et al. 2012, 2023; Buitrago et al. 2013; Huertas-Company et al. 2014; Kartaltepe et al. 2015; Ferreira et al. 2023). Given its correlation with multiple galactic properties in the local universe, morphology can be a valuable tracer of the evolution of galaxies, and a key to understanding the physical processes that drive said evolution. By examining morphology across a span of redshifts and environments, astronomers have had the unique opportunity to answer the question of whether galaxy evolution is driven primarily by "nature" or "nurture".

1.2 The emergence of the morphology-density relation

One method to assess the impact of environment ("nurture") on galaxy evolution is to study how morphology varies between low-density and high-density environments. Early studies explore this topic using dense galaxy clusters and examining how typical galaxy morphologies change with distance from the cluster center, also known as the morphology-radius relation (e.g. Melnick & Sargent 1977). However, clusters are not all consistent in terms of size, density, or even symmetry, and there are many irregular and non-relaxed clusters for which the location of the cluster center is highly uncertain and difficult to define. Dressler (1980) addresses this problem by studying morphology as a function of local galaxy density,

allowing him to examine the relationship in both regular and irregular cluster environments. His is the first flagship study of what is now known as the morphology-density relation.

Dressler (1980) utilizes a large sample of 55 rich galaxy clusters in the nearby universe ($z \lesssim 0.06$), imaged on physical photographic plates. He finds the fractions of each morphological type in the low-density field by counting galaxies from 15 plates with random sky positions, which are used for both comparison and statistical background subtraction. He classifies morphologies through visual inspection, calculating the fractions of elliptical galaxies (E), lenticular galaxies (S0), and spiral or irregular galaxies (Sp+Irr). Dressler (1980) also uses a method called Nth-Nearest Neighbours, in which he calculates the projected local density of any galaxy within a square 2D area containing its $N = 10$ nearest neighbouring galaxies. He finds that as local density increases, the fraction of Sp+Irr galaxies decreases, while the fraction of E and S0 galaxies both increase. To date, Dressler (1980) remains one of the most influential papers on the morphology-density relation, and a strong piece of evidence for the role of environment in galactic evolution.

Dressler et al. (1997) return to the morphology-density relation by studying galaxies at $z \sim 0.5$ using newly obtained data from the *Hubble Space Telescope* (*HST*). They use a sample of 10 clusters from $0.36 < z < 0.57$, imaged in filters corresponding to the rest-frame B-band of the cluster galaxies, following largely the same methodology as Dressler (1980). Dressler et al. (1997) also re-evaluate the data from Dressler (1980), making slight corrections, but allowing them to compare the morphology-density relation between the local universe and $z \sim 0.5$. Overall, they find that the trends are qualitatively similar, but that the fraction of S0 galaxies is 2-3 times smaller at $z \sim 0.5$ than locally, while the fraction of Sp galaxies is larger. Dressler et al. (1997) also compare between centrally-concentrated regular clusters vs lower density irregular clusters, finding that the morphology-density relation is stronger in high-density clusters and weaker or non-existent in irregular clusters. With the aid of the $z \sim 0.5$ sample, Dressler et al. (1997) also suggest that the formation of elliptical galaxies may be independent of the virialization status of the cluster.

In a third flagship study, Postman et al. (2005) extend the relation to galaxies at $z \sim 1$ with comparative methods. Their sample consists of 7 clusters from $0.83 < z < 1.27$, with observations of each cluster in at least two filters from the *HST* Advanced Camera for Surveys (ACS) Wide-Field Camera (WFC). All morphological classifications are done by

visual inspection in the rest-frame B-band, as in previous studies. Postman et al. (2005) assess their methods, including comparison of different calculations of local density, as well as the validity of comparing cluster fractions calculated with statistical background subtraction vs redshift-selection. Using 7th-Nearest Neighbours, they calculate local densities including weighting and correction schemes to directly compare to the lower redshift results of Dressler (1980) and Dressler et al. (1997). As shown in Figure 1.2, they find that the morphology-density relation is in place as early as $z \sim 1$, but that the S0 fraction is once again smaller than low redshifts with a very weak dependence on density. The combined E+S0 fraction does not increase as steeply at higher densities in $z \sim 1$ as it does for lower redshifts. Postman et al. (2005) conclude that the observed evolution in the morphology-density relation between $z = 0$ and $z = 1$ is driven primarily by an evolution in the S0 and Sp populations.

1.3 The universe at cosmic noon

Studies of galactic evolution have revealed an interesting period in the history of the universe. Spanning roughly $1 < z < 3$, the epoch of cosmic noon is a time period where the star formation rate (SFR) of galaxies peaked on a universal scale. It is estimated that up to half of the stars in present-day galaxies were formed during this time (Förster Schreiber & Wuyts 2020). SFR is only one of the galaxy properties found to be different during this time. Observationally, galaxies at high-z are found to be smaller and more compact (Mei et al. 2012; van der Wel et al. 2014), clumpier (Wuyts et al. 2012; Gillman et al. 2020), more asymmetrical (Huertas-Company et al. 2014; Ferreira et al. 2023), bluer with higher SFRs (Kajisawa & Yamada 2006), have lower metallicities (Maiolino & Mannucci 2019), and have larger reservoirs of cold molecular gas (Tacconi et al. 2020). Morphologically, high-z galaxies are also more disturbed and peculiar at higher redshifts, suggesting a higher frequency of mergers and interactions (Gillman et al. 2020; Ferreira et al. 2023). Buitrago et al. (2013) find that early-type morphologies may only comprise the majority of the galaxy population since $z \sim 1$, while late-type and peculiar galaxies are the predominant morphologies during cosmic noon.

It is not only galaxies that are different at cosmic noon, but also the environments they

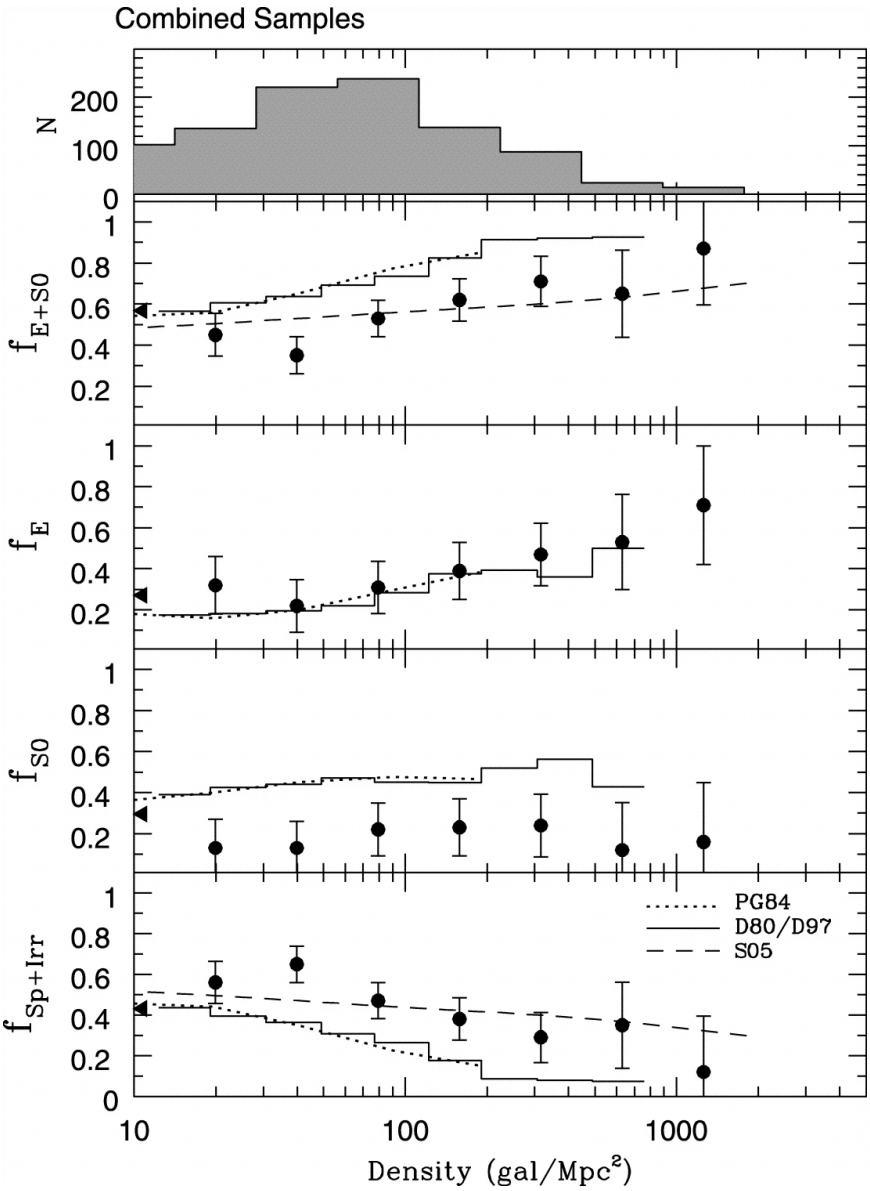

Figure 1.2: The morphology-density relation as in Postman et al. (2005), showing results from their clusters at $z \sim 1$ (circles with error bars) in comparison to studies of galaxies at $z \sim 0$ (dotted line and solid lines) and another study at $z \sim 1$ (dashed line). The y-axis expresses the relative number of each visual morphological type as a fraction of the total for a given local galaxy density.

lived in. Cosmic noon is also the epoch when early-universe protoclusters began to collapse into modern day galaxy clusters (Chiang et al. 2013; Overzier 2016). A protocluster can be loosely defined as an overdensity in cosmic space that will eventually transform into a virialized cluster, often defined as having a mass of at least $10^{14} M_{\odot}$. While modern day clusters generally consist of a central dominant dark matter halo, protoclusters at $z > 2$ often consist of multiple smaller dark matter halos (Overzier 2016). Using cosmological simulations to study cluster progenitors, Chiang et al. (2013) find that protoclusters between $2 < z < 5$ are more extended, often having larger radii than their future $z = 0$ clusters. Despite lower average densities and lack of a dominant dark matter halo, protoclusters are still found to host higher fractions of quenched galaxies than the field at all redshifts (Muldrew et al. 2018). While the overall SFR is predicted to have peaked at roughly $z \sim 2$ in the field, Muldrew et al. (2018) find that star formation in the protoclusters peaked earlier at $z \sim 2.6$, suggesting that galaxies in protoclusters typically stop forming stars at earlier cosmic times than galaxies in the field.

Cosmic noon also has the potential to reveal important clues in the evolution of the morphology-density relation, and the physical properties that drive it. Astronomers still do not know how long the morphology-density relation has been in place, and each step back in the past can help us understand its origin. Newly-formed cluster and protocluster environments may be dominated by different physical processes than the evolved clusters of today. A careful study of how morphology varies in these environments, within the context of overall morphological evolution during this epoch, could greatly expand our understanding of galaxy evolution.

1.4 Alternative morphology classifications

With advancements in digital astronomy, a number of different techniques have become common to assist in classifying galaxy morphology without the need for manual visual classification. These techniques not only save time over visual classifications, but most can also turn galaxy morphology from a qualitative assessment into a quantitative measurement. The two main classes of quantitative morphological techniques are parametric and non-parametric. Parametric techniques are based upon a prior assumption that the light in

galaxies, on average, follows a particular distribution. Non-parametric techniques, on the other hand, do not rely on prior assumptions of the light distribution. Please note that we will be using structure and morphology interchangeably in this section and much of the thesis, but will return to a discussion on the difference between the two in Section 5.1.

The most common parametric technique is profile fitting, in which the observed 2D light profile of a galaxy is fit to an analytical model. The Sérsic profile is an expression of light intensity with radius, where the general structure of a galaxy can be quantified by a single parameter called the Sérsic index, n (Sersic 1968). Most notably, a value of $n = 1$ reproduces an exponential profile that is well-fit to galaxy disks (Freeman 1970), while a value of $n = 4$ reproduces a de Vaucouleurs profile that approximates many elliptical galaxies (de Vaucouleurs 1948). Single-component Sérsic fits, which attempt to model all of a galaxy's light with a single profile, have been effectively used to measure galaxy sizes and to quantify their morphological structure through n (e.g. van der Wel 2008; van der Wel et al. 2012; Harrison et al. 2017; Matharu et al. 2019; Gillman et al. 2020; Sazonova et al. 2020). Multi-component Sérsic fitting may be a better fit to some galaxies where the outer light follows a different distribution than the core, and can be used for samples with higher resolution and signal-to-noise ratio, S/N (e.g. Ascaso et al. 2009; Nantais et al. 2013). Since 2D Sérsic profiles are modelled as ellipses to the observed galaxy, some studies have even quantified morphology using the axis ratio from a Sérsic fit (Chan et al. 2021).

Another common parametric technique is bulge-disk decomposition, where the overall light of a galaxy is assumed to be the sum of the light from its disk and the light from its central bulge. This requires modelling the disk and bulge separately, which is usually achieved by either a two-component Sérsic fit or by fixing one or both components to an assumed distribution, such as fitting the disk to an exponential profile or the bulge to a de Vaucouleurs profile. The structure of the galaxy can then be quantified by the bulge strength or B/T, the ratio of light contained in the bulge compared to that of the whole galaxy (e.g. Simard et al. 2011; Cerulo et al. 2017; Gao et al. 2018; Bluck et al. 2019; Gillman et al. 2020). Early-type galaxies often have high B/T due to a lack of outer disk or dominant central bulge, while late-type galaxies have low B/T.

Non-parametric techniques have been found to reasonably separate galaxy morphologies when considering multiple measurements together, rather than a single parameter. The most

common of these is the CAS system, which stands for concentration (C), asymmetry (A), and clumpiness (or smoothness, S) (Conselice 2003). Concentration is a ratio between the size of two annuli containing different amounts of the galaxy's total light (often 50 and 80 percent), while measurements of asymmetry and clumpiness involve subtracting a rotated or blurred version of the galaxy image from itself and measuring the residual light. In images with good resolution and high S/N, high asymmetry and clumpiness can help identify non-central star formation or spiral arms. Another non-parametric method that has gained popularity is the combination of Gini index and M_{20} (Abraham et al. 2003; Lotz et al. 2004). The Gini index was adapted from economics, and in astronomy it quantifies how evenly-distributed the light is amongst pixels in a galaxy image. M_{20} is the second-order moment of the brightest pixels containing 20 percent of the galaxy's total light, calculated using the flux of each pixel and its squared distance from the galaxy center. Gini$-M_{20}$ is particularly useful for identifying galaxy mergers. While some studies use the CAS system on its own (e.g. Gillman et al. 2020), Gini$-M_{20}$ is often used in combination with the CAS system (e.g. Cassata et al. 2007; Tasca et al. 2009; Sazonova et al. 2020; Ferreira et al. 2023).

We have covered some of the more popular quantitative methods for quantifying galaxy structure, but ours is far from a complete list of techniques. Some studies have measured galaxy morphology using a modification of the techniques listed above, such as Goto et al. (2003) who use parameters *Cin* and *Tauto* based largely on concentration, or van der Wel et al. (2007) and van der Wel (2008) who use a combination of Sérsic index and a parameter that measures galaxy "bumpiness". In more recent years, the use of artificial intelligence has become popular for morphological classification, by utilizing deep learning to reduce parameter space from a wide range of structural measurements (e.g. Huertas-Company et al. 2008; Cerulo et al. 2017), or by replacing human classifiers with machine learning trained on a set of previously visually classified galaxies (e.g. Cavanagh et al. 2023; Pfeffer et al. 2023). Other studies have even looked outside of the realm of light and mass profiles, and have been successful in using kinematic measurements to classify galaxy disks and identify sub-populations within them (e.g. Gillman et al. 2020; Joshi et al. 2020). While each technique has its own strengths, it is clear we are entering an age where manual visual classification need not be the default method for studying galaxy morphology.

1.5 Motivation and outline

This thesis is motivated by two main goals. Our first goal is to extend our understanding of the morphology-density relation into the late epoch of cosmic noon. Using a mix of spectroscopic and photometric redshifts, we aim to be one of the first studies of this kind to have high accuracy in both our sample and density measurements. By studying $z \sim 1.6$, we can probe not only a higher redshift than previous major studies, but also enter the transitional period between modern-day clusters and early-universe protoclusters. Our second goal is to improve upon the methods used for studying the morphology-density relation, in particular to improve the efficiency and consistency with which we classify galaxy morphology. Ideally, we would like to develop a quantitative method for classifying morphology that can be applied easily, equitably, and quickly to large samples of galaxies.

We have chosen a sample of three spectroscopically-confirmed galaxy clusters at $1.594 < z < 1.633$ from the SpARCS collaboration (Muzzin et al. 2009; Wilson et al. 2009). These clusters each have a wealth of photometric observations, spectroscopy of some cluster members, and grism coverage, which make them ideal for our proposed study. Obtaining spectroscopic and grism redshifts where we can is important, as accurate redshifts can influence not only cluster membership but also local density calculations. We build a comparative sample of galaxies residing in low-density environments at a similar redshift, using the COSMOS and GOODS-S fields from 3D-HST/CANDELS (Grogin et al. 2011; Koekemoer et al. 2011). These fields in particular are a good fit for our study due to deep photometric observations in the same primary filter as our clusters, allowing for detection of field galaxies at $z \sim 1.6$, as well as a large amount grism coverage and redshift estimates. A further advantage to these fields is that van der Wel et al. (2012) have already catalogued galaxy structure in these fields using a similar method to our own, which will allow for easy comparison between environments. Chapter 2 covers the full details on our chosen clusters, fields, and sample selection process.

As suggested by the name of the relation, this study predominantly involves measuring quantitative galaxy morphologies and calculating local densities. We use the GALFIT algorithm (Peng et al. 2002, 2010a) to automatically fit 2D Sérsic profiles to images of our

cluster galaxies. We use the Sérsic index obtained from these fits as a quantitative measurement of morphology that reasonably separates disk-like and bulge-like galaxies, which we use in place of visual spiral/late-type and elliptical/early-type classifications. To increase the accuracy of our sample's redshifts, we reduce G102 grism spectra of our clusters and obtain grism redshifts for galaxies which lack other spectroscopic redshift measurements. We opt to use the Nth-Nearest Neighbours method as a simple yet robust way to calculate local densities, increasing our accuracy over previous studies by using redshift/velocity cuts as in Cooper et al. (2005), who demonstrate the effectiveness of using Nth-Nearest Neighbours to calculate densities of $z > 1$ galaxies. Further details on our methodology are outlined in Chapter 3.

Chapter 4 presents our results, most notably the observed morphology-density relation at $z \sim 1.6$ with a direct comparison between cluster and field environments. We conduct additional analysis of the morphology-mass relation, to explore whether the observed relation with local density is directly influenced by environment, or whether it is potentially an indirect relation driven by primarily by differences in stellar mass. We also confirm the stellar size-mass relation and look at the effect of cluster and field environments on galaxy colours for each morphological type.

We discuss the impact and interpretation of our results in Chapter 5, and summarize our conclusions in Chapter 6. We adopt a ΛCDM cosmology with $H_0 = 70$ km s^{-1} Mpc^{-1}, $\Omega_m = 0.3$, and $\Omega_\Lambda = 0.7$.

Chapter 2

Data Sample

To properly study the relationship between morphology and local density, we require a sample of galaxies from similar redshifts in both high-density (cluster) and low-density (field) environments. The following sections outline our cluster sample, consisting of three $z \sim 1.6$ clusters from the SpARCS collaboration, and our field sample, consisting of two fields from 3D-HST/CANDELS. We also discuss our completeness limits and galaxy sample selection.

2.1 Cluster sample

2.1.1 The SpARCS collaboration

Our chosen galaxy clusters come from the *Spitzer* Adaptation of the Red-sequence Cluster Survey (SpARCS) (Muzzin et al. 2009; Wilson et al. 2009). With a goal of detecting a large homogeneous sample of $z \sim 1$ galaxy clusters, SpARCS utilized existing observations of the *Spitzer* Wide-Area Infrared Extragalactic Survey (SWIRE) Legacy fields to find cluster candidates. Their initial method utilized $z' - 3.6\ \mu$m colours to detect clusters up to $z \sim 1.4$, with tight constraints on photometric redshift estimates of the galaxies. SpARCS detected hundreds of $z > 1$ cluster candidates with this method, including a selection of spectroscopically-confirmed galaxy clusters within $0.85 < z < 1.35$.

Following their success at finding $z \sim 1$ clusters, the SpARCS team developed an additional method for reliable detection of clusters at $z > 1.4$. As outlined in Muzzin

Cluster	Nickname	RA	Dec	Redshift	F160W exposure time
J033056-284300	CDFS44	03:30:55.9	-28:42:59.5	1.626	5019 s
J022546-035517	XMM105	02:25:45.6	-03:55:17.1	1.594	2424 s
J022426-032330	XMM113	02:24:26.3	-03:23:30.8	1.633	6116 s

Table 2.1: Overview of all three clusters selected for this study.

et al. (2013), the stellar bump sequence utilizes a bump in the spectral energy distribution (SED) of galaxies at rest-frame wavelengths of 1.6 μm, which is indicative of stellar populations older than 10 Myr. For $z < 1.7$, this feature can be used to identify galaxy overdensities through a combination of 3.6 μm−4.5 μm colours and a $z' - 3.6$ μm colour cut, with reasonably tight photometric redshift estimates. This method lead to the detection and spectroscopic-confirmation of 5 additional clusters in the SWIRE Legacy fields at $1.594 < z < 1.708$.

We use three spectroscopically-confirmed SpARCS clusters for this study: J033056-284300 (nicknamed CDFS44) at $z = 1.626$, J022546-035517 (nicknamed XMM105) at $z = 1.594$, and J022426-032330 (nicknamed XMM113) at $z = 1.633$. XMM113 and CDFS44 were first utilized in Lidman et al. (2012) alongside lower redshift SpARCS clusters, while spectroscopic confirmation of XMM113 was announced in Muzzin et al. (2013). The first introduction of XMM105 later followed in Nantais et al. (2016). An overview of each cluster is given in Table 2.1.

2.1.2 Cluster catalogs and photometry

We primarily utilize the most recent photometric catalogs for each cluster, cross-referencing with catalogs of the spectroscopic data only when determining best redshift estimates. We refer the reader to Nantais et al. (2016) and Nantais et al. (2020) for a full discussion on the creation of the photometric catalogs.

Cluster photometry includes $u'g'r'i'z'$ coverage by Magellan IMACS for CDFS44 and

XMM113, and the same filter coverage by CFHT MegaCam for XMM105. All three clusters have Y coverage from VLT HAWK-I, while CDFS44 and XMM113 also have additional coverage in J. CDFS44 and XMM113 have *HST* WFC3 coverage in F814W, as well as WFC3/IR coverage in F105W and F140W. All three clusters have coverage in WFC3/IR F160W (the primary filter used in this study). All three clusters also have coverage in infrared from *Spitzer* IRAC in [3.6] [4.5] [5.8] [8.0], as well as MIPS in [24]. Coverage in [12] comes from WISE. Additionally, they have coverage from Herschel PACS in [110] [160], and SPIRE in [250] [350] [500].

The extensive photometric coverage helps produce detailed SEDs of galaxies in each cluster. The photometric catalogs include photometric redshifts and rest-frame *UVJ* colours from EAZY (Brammer et al. 2008), as well as galaxy stellar masses calculated with FAST (Kriek et al. 2009). All three clusters have ground-based spectroscopy of a limited number of galaxies from Keck/MOSFIRE in near-infrared, as well as optical spectroscopy from VLT/FORS2. Where we can, we utilize the spectroscopic redshifts obtained from these observations for improved accuracy. Each cluster also has *HST* grism spectra observations in G102 to a depth of 4 orbits.

At $z \sim 1.6$, the F160W filter covers a rest-frame wavelength of roughly 550 – 650 nm, equivalent to the rest-frame optical V-band. We utilize drizzled F160W images of each cluster for our morphological measurements, which have been reduced to a plate scale of $0.06''$/px. The total exposure time for each cluster is listed in Table 2.1, while the F160W coverage of each cluster is shown in Figure 2.1. We note that the $0.06''$/px reduction of XMM105 was performed separately from the other two clusters, and that the shorter exposure time also results in a higher level of background noise for this cluster. The fields of view cover areas of roughly $2'\times2'$ targeted at the center of each cluster, which is smaller than the total sky coverage of the clusters as observed in ground-based images. Some objects in the catalogs, including spectroscopically-confirmed cluster members, lie beyond the bounds of the F160W image, and therefore cannot be included directly in our analysis.

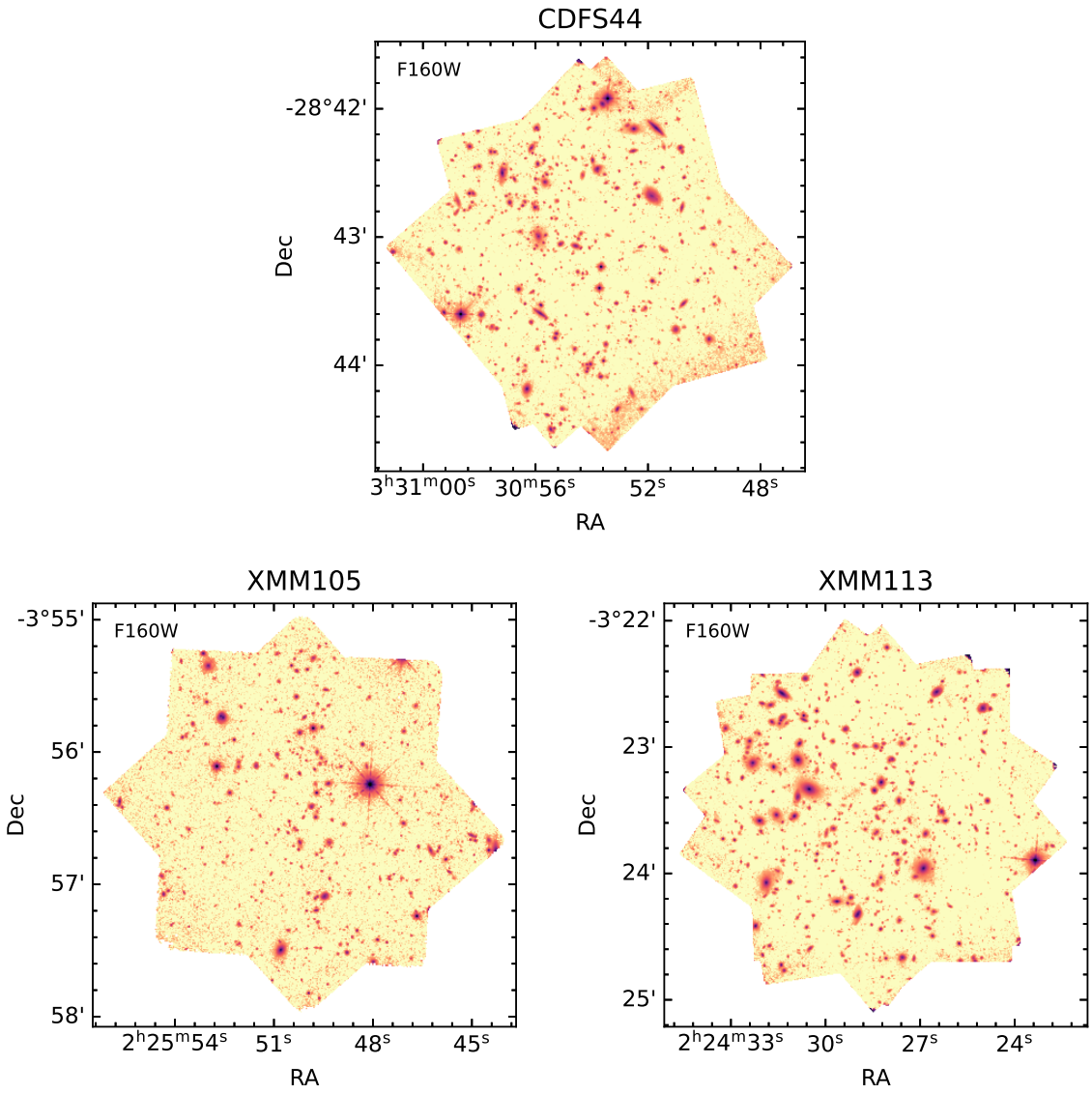

Figure 2.1: F160W coverage of all 3 clusters: CDFS44 (top), XMM105 (bottom left), and XMM113 (bottom right). Note that the HST F160W coverage only captures the central region of each cluster.

2.1.3 Grism spectroscopy

Grism spectroscopy, also known as slitless spectroscopy, is a method that can be used to obtain spectra of many objects all at once, at the expense of lower resolution and higher rates of possible spectra contamination compared to traditional slit-based spectroscopy. A grism is a combination of both a grating and a prism, which work in combination to separate incoming light and disperse it horizontally depending on its wavelength. Since grisms do not require barriers or slits of any kind, grism observations result in an entire field of view in which the light from all objects are smeared in wavelength relative to their on-sky positions. These smears constitute the spectra themselves, and are analyzed by separating 2D spectral traces of each individual object. Taking grism observations from two position angles helps minimize contamination from multiple object traces overlapping with each other. The resolution of grism spectroscopy is necessarily limited by how light from extended sources overlaps with itself within the spectral trace.

All three clusters in our sample have 4-orbit depth spectra from the G102 grism on WFC3 (GO-13306; PI Wilson). G102 covers an observed wavelength range of 800 – 1150 nm, with a resolving power of 210 at 1000 nm and a dispersion of 2.45 nm/pixel. While the observed wavelength range is small, it covers two prominent spectral features at $z \sim 1.6$ which can be used to confirm the redshift of galaxies. The 4000Å break is a feature in the spectra of many galaxies, but is dominant in those with older stellar populations, making it especially useful in determining the redshift of quiescent galaxies which lack strong emission lines. The [OII] emission line doublet (rest-frame $\lambda\lambda 3726 - 3729$Å) is caused by the presence of younger stellar populations, which can make it a strong spectral feature in star-forming galaxies. At $z \sim 1.6$, these features shift to observed wavelengths of 1050 nm and approximately 970 nm, respectively, which both fall comfortably within the range of G102. For our purposes, this data offers a chance to obtain higher-accuracy redshifts for many objects in and around our clusters which do not have ground-based spectra.

2.2 Field sample

2.2.1 3D-HST/CANDELS

Our field sample comes from 3D-HST/CANDELS (Grogin et al. 2011; Koekemoer et al. 2011). The Cosmic Assembly Near-IR Deep Extragalactic Legacy Survey (CANDELS) was designed to facilitate study of galaxy evolution from $z = 8 - 1.5$, by obtaining approximately 720 arcmin^2 of near-IR photometry with *HST* WFC3 and ACS in five fields: GOODS-N, GOODS-S, UDS, EDS/AEGIS, and COSMOS. In addition to this, CANDELS has obtained approximately 120 arcmin^2 of deep imaging in GOODS-N and GOODS-S. 3D-HST supplements the CANDELS observations with near-IR grism spectroscopy using WFC3 G141 and ACS G800L in the same five fields, optimized for the study of galaxies at cosmic noon around $1 < z < 3$. 3D-HST has obtained redshifts, spectra, stellar masses, SFRs, and rest-frame colours for a large number of galaxies across all five fields.

Together, 3D-HST and CANDELS represent the largest *HST* survey to date, and their fields are among the most widely-studied for high-redshift galaxy evolution. Their wide area, wealth of ancillary data, and depth make the 3D-HST/CANDELS fields particularly well-suited as counterpart field samples to our $z \sim 1.6$ clusters.

2.2.2 COSMOS and GOODS-S fields

We select the COSMOS and GOODS-S for our comparative field sample. These fields were chosen primarily for their wealth of additional data and filter coverage. We show the F160W mosaic coverage and exposures in Figure 2.2 for COSMOS and Figure 2.3 for GOODS-S (Skelton et al. 2014; Grogin et al. 2011; Koekemoer et al. 2011). We use the 3D-HST catalogs for most properties of our field galaxies, including sky positions, F160W fluxes, stellar masses, and rest-frame colours (Brammer et al. 2012; Skelton et al. 2014). For each galaxy, we use the best redshift measurement from the linematched grism catalogs (Brammer et al. 2012; Momcheva et al. 2016). We also record whether the source of the best redshift measurement is ground-based spectroscopy, G141 grism, or photometry.

We use Sérsic profile fits from van der Wel et al. (2012) for our COSMOS and GOODS-S field galaxies. Single-component Sérsic profiles were fit to cutouts of each galaxy in F160W

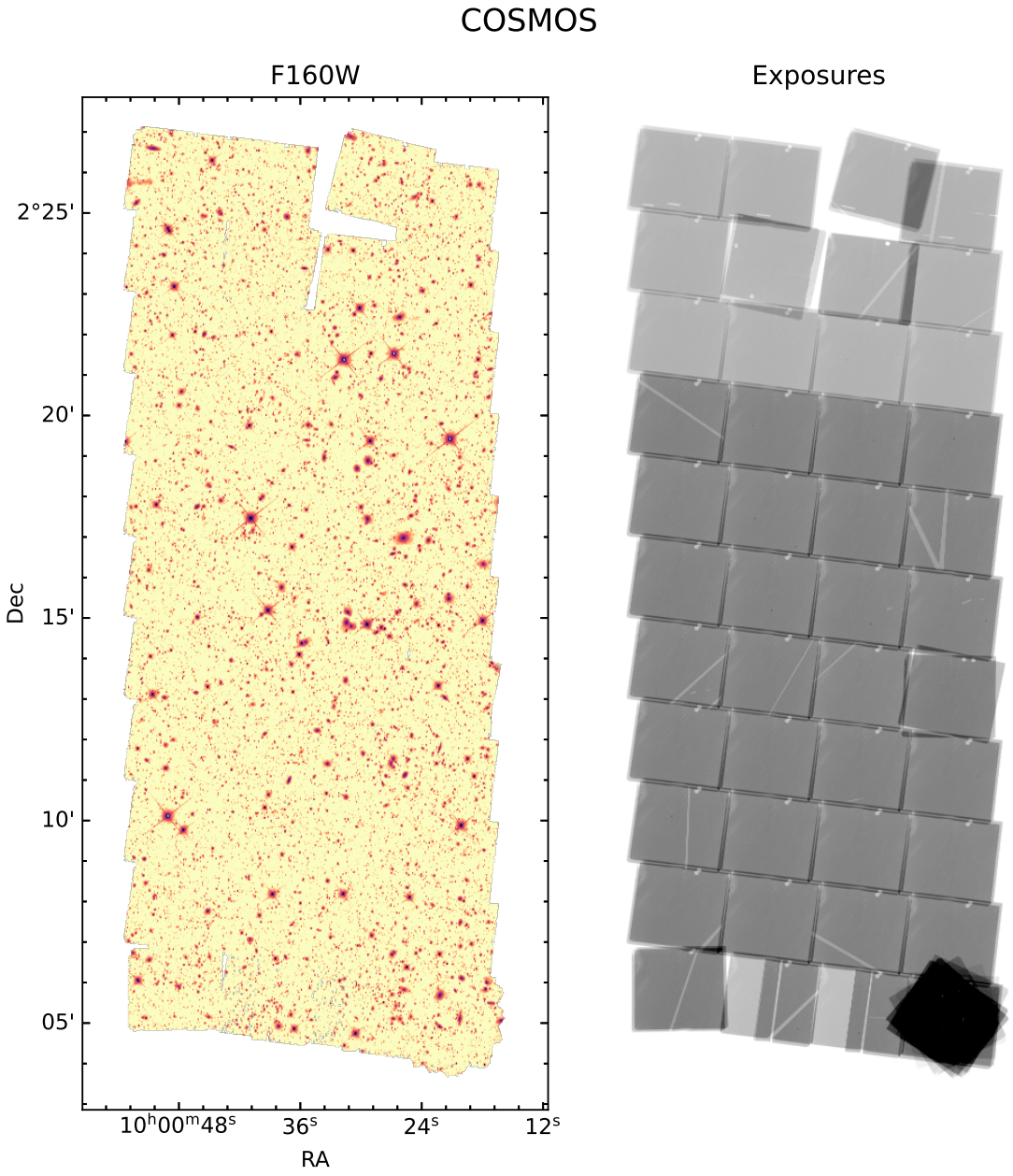

Figure 2.2: F160W mosaic (left) and relative exposure time (right) for the COSMOS field.

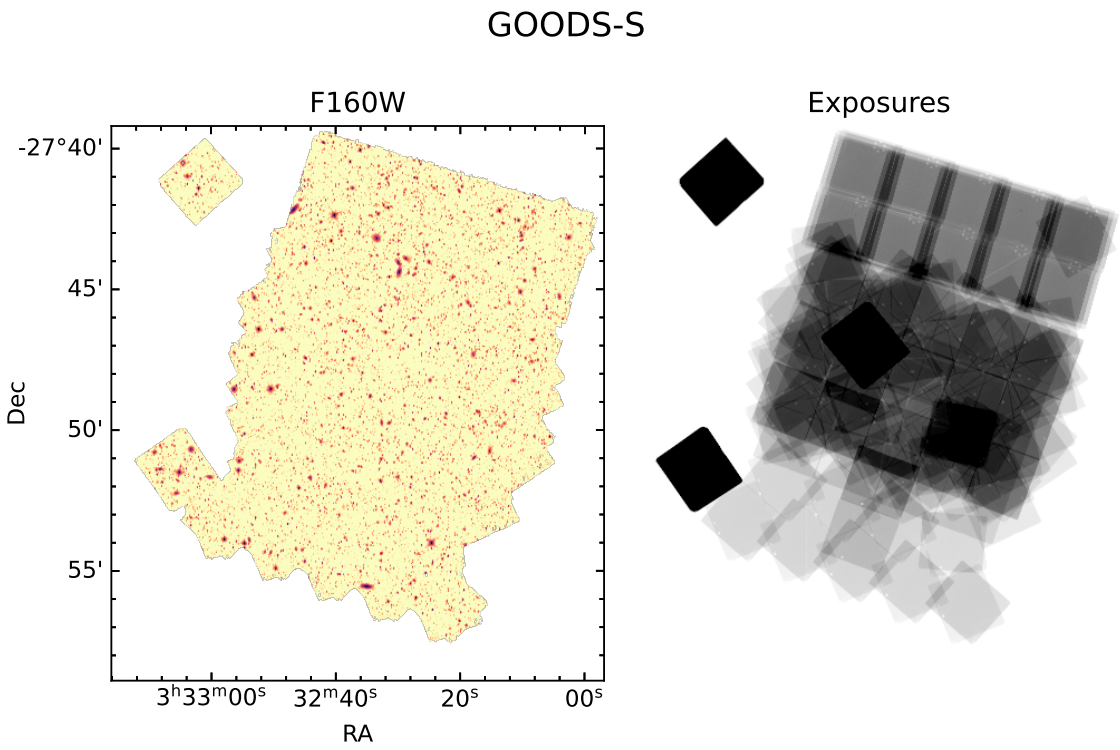

Figure 2.3: F160W mosaic (left) and relative exposure time (right) for the GOODS-S field.

using GALAPAGOS (Barden et al. 2012), an IDL-based wrapper for GALFIT. We only use Sérsic parameters for galaxies which have a quality flag of 0, indicating good and reliable fits. Galaxies without good fits are still kept in the field sample as possible neighbours, however they are not included in morphological analysis.

Going forward, the methods discussed in Chapter 3 for determining best redshift and fitting Sérsic profiles are only applied to the cluster galaxies, while we use the cataloged values for the field galaxies as described here.

2.3 Sample selection

2.3.1 Completeness limits

The F160W images used in our study are reduced to a finer pixel scale than used in previous studies of our clusters. As such, it is necessary to determine the completeness limits for

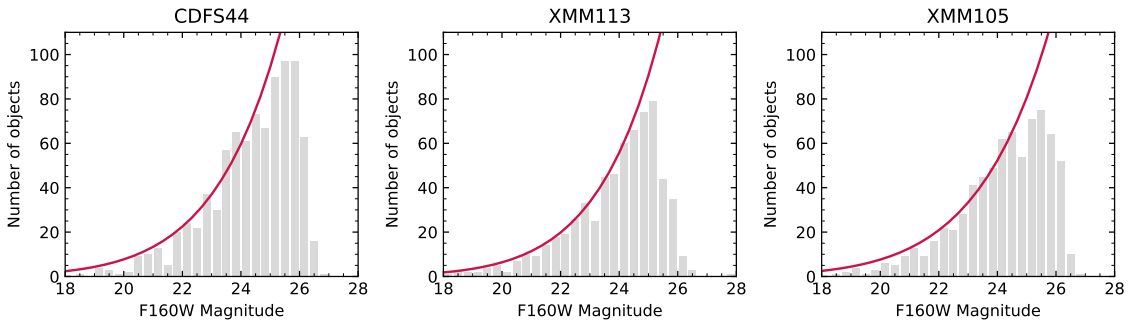

Figure 2.4: An example of the plots used to determine the magnitude completeness limit of each cluster. The number count of objects is plotted as a histogram by their F160W magnitude, while the curve is a power law fit to the histogram data (excluding the faintest magnitudes where the number count of objects begins to decline).

object detection in our images. We will then use this to create a sample of mass-complete members across our three clusters.

In each cluster, we plot a histogram of the F160W magnitude of all objects. We fit a power law to the histogram data, excluding the faintest magnitudes where the number count of objects begins to decline. Assuming the power law is an estimate of the true number counts of all objects, we compare this fit to the histogram data to determine the magnitude at which approximately 80 percent of objects are detected. We repeat this method with varied histogram bin sizes to obtain a more accurate estimate of the 80 percent magnitude limit for each cluster. An example of this is shown in Figure 2.4.

Next, we convert the magnitude limits into corresponding stellar masses limits. In each cluster, we collect all galaxies which have photometric redshifts within $1.4 < z_{phot} < 1.8$ and are 1 ± 0.2 magnitudes brighter than the magnitude limit, where we are confident that our sample is complete. We set $M_{*,90}$ to be the 90th percentile in stellar mass of these objects (i.e. where 90 percent of these objects have masses below $M_{*,90}$). By assuming a constant mass-to-light ratio, we then use equation 2.1 to calculate $M_{*,lim}$, the equivalent stellar mass limit at our 80 percent magnitude limit. This is a reasonable assumption for our purposes as the stellar mass-to-light ratio of galaxies should not change significantly over 1 magnitude.

$$M_{*,lim} = M_{*,90} \times 10^{-0.4} \tag{2.1}$$

We find stellar mass limits of $10^{9.47} M_{\odot}$ in CDFS44, $10^{9.50} M_{\odot}$ in XMM105, and $10^{9.58} M_{\odot}$ in XMM113. Since we will be combining the data from all clusters together, we take the highest mass limit of the three to be our overall mass limit. As the field data is at least as deep as the cluster data in F160W, we choose not to compute separate mass completeness limits for the field. We therefore assume our cluster and field samples are at least 80 percent complete for stellar masses above $10^{9.58} M_{\odot}$.

2.3.2 Cluster membership

We begin by creating cluster samples that contain all objects from the photometric cluster catalogs with a stellar mass greater than $10^{8} M_{\odot}$ and a non-zero photometric redshift estimate. This helps to ensure that every object in our sample is a galaxy with decent photometry.

When selecting galaxies as potential cluster members from our cluster sample, we require they have a measured flux in F160W as well as a stellar mass greater than our mass completeness limit of $10^{9.58} M_{\odot}$. Measured F160W flux is crucial as it ensures the galaxy was properly detected and lies within the field of view of the F160W image. If this is not the case, then we will not be able to measure its morphology.

Our third requirement is that cluster members must lie within the redshift range of the cluster based on their best redshift estimate. The size of typical uncertainties in redshift measurements vary greatly between the method used to estimate the redshift. Redshifts calculated from traditional slit-based spectroscopy often have the smallest uncertainties, followed by grism redshifts which are more uncertain due to lower spectral resolution. Photometric redshifts have the highest associated errors and uncertainties, since the redshift can only be estimated from the overall shape of the SED and not from the detection of specific spectral features. We refer the reader to van der Burg et al. (2013) and Matharu et al. (2019) who assess the typical rates of false positive and false negative cluster members based on different redshift estimates at $z \sim 1$.

We use the following formulae to identify cluster members based on their best redshift estimate. We define the redshift of the cluster to be z_{cl}. When selecting cluster members based on their spectroscopic redshift, z_{spec}, we use values as in Muzzin et al. (2012):

$$\Delta z_{spec} = \left| \frac{z_{spec} - z_{cl}}{1 + z_{cl}} \right| \leq 0.005 \tag{2.2}$$

We select cluster members based on their grism redshift, z_{grism}, using the values found by Matharu et al. (2019):

$$\Delta z_{grism} = \left| \frac{z_{grism} - z_{cl}}{1 + z_{cl}} \right| \leq 0.02 \tag{2.3}$$

Finally, we select cluster members based on the photometric redshift, z_{phot}, following the values in van der Burg et al. (2013) and Nantais et al. (2016):

$$\Delta z_{phot} = \left| \frac{z_{phot} - z_{cl}}{1 + z_{cl}} \right| \leq 0.05 \tag{2.4}$$

Galaxies which are not chosen as cluster members are still kept within the cluster sample as potential neighbours for calculating local density. We note that this includes galaxies which have no measured F160W flux, indicating that they were undetected or lie outside of the F160W field of view. This is an intentional choice. As the F160W field of view covers only the central $2' \times 2'$ area of the cluster, it misses multiple spectroscopically-confirmed cluster members that have been found in wider ground-based observations. While we cannot include these galaxies in our own cluster member selection due to being unable to measure their F160W morphologies, they can still act as valid neighbours to our selected cluster members.

In Section 3.1.2, we describe the process of choosing the best redshift estimates and outline the number of cluster members found in our samples.

2.3.3 Field membership

One of our goals is to create a sample of field galaxies such that we can directly compare the results between cluster and field environments. Many previous studies have restricted their consideration of field galaxies to obtaining overall morphological fractions, which they mainly use to plot a single field point on the lowest end of their density scale and/or to calculate field corrections to their cluster populations. We intend to analyse our field galaxies in the same ways as our cluster galaxies, which means we must construct our field sample in a similar way.

As with the cluster sample, we begin by creating a sample of field objects from the COSMOS and GOODS-S catalogs with stellar masses greater than $10^8 M_\odot$ and photometric redshift estimates. From there, we designate galaxies in our sample as "field members" (to match cluster terminology) if they meet criteria equivalent to our selected cluster members. Field members will be used as direct comparison to cluster members throughout this study, so it is important to select them using similar requirements. We require all field members to have a measured flux in F160W and a minimum stellar mass of $10^{9.58} M_\odot$, to agree with the stellar mass limits of our clusters.

Unlike clusters, fields do not have a unique redshift which can be used to define "membership". In essence, we wish to select field members which would have passed redshift selection for any of our three clusters. As our clusters are close in redshift, in practice it is easier to require that the best redshift of any field member lie between the upper-most and lower-most bounds of our three clusters.

We use the following ranges to determine field membership, depending on whether the galaxy's best redshift estimate is z_{spec}, z_{grism}, or z_{phot}. The values in each range are calculated from equations 2.2 through 2.4. The lower bounds are found by taking the lower-most bounds of cluster membership set by $z_{cl} = 1.594$, while the upper bounds are found by taking the upper-most bounds of cluster membership set by $z_{cl} = 1.633$. Best redshift measurements for field galaxies come from the COSMOS and GOODS-S catalogs as outlined in Section 2.2.

$$1.58103 \leq z_{spec} \leq 1.646165 \tag{2.5}$$

$$1.54212 \leq z_{grism} \leq 1.68566 \tag{2.6}$$

$$1.4643 \leq z_{phot} \leq 1.76465 \tag{2.7}$$

The number of field members found is given in Section 3.1.2.

Chapter 3

Methodology

3.1 Redshift estimates

3.1.1 Fitting grism redshifts with grizli

In order to take advantage of the improved accuracy that comes with grism redshifts, we first reduce the G102 data of our clusters using grizli, a software developed for grism redshift and line analysis of space-based slitless spectroscopy (Brammer 2019). The grizli pipeline is designed to run in Python, with the ability to query and retrieve *HST* grism exposures and process the data from end-to-end. It includes automatic preprocessing steps such as matching visits, background subtraction, field flattening, creation of drizzled mosaics of both grism spectra and matching direct imaging, and creation of object catalogs and segmentation maps.

On the first run of the grizli pipeline, it is necessary to process the grism spectra without including any ancillary photometric data. grizli uses traces of the objects to model the object continuum and background contamination (such as from neighbouring objects or spurious detections) separately. It considers each exposure and both grism position angles when modelling the contamination, which improves its ability to accurately separate the spectra of different objects. By utilizing the grizli catalog created from the corresponding direct detection image, we then extract the 2D spectra of individual objects from the full grism field of view. grizli can then model and fit the spectrum of each object, producing a 1D

spectrum and fitting a redshift to the observed spectral features.

Due to the small wavelength range of G102, it can be difficult for grizli to accurately predict the shape of an entire galaxy SED from the grism spectrum alone. At this stage, we assume any grism redshift estimates to be highly uncertain and not reliable. Following the first run, we then pass our grizli fits through the pipeline again, this time including all known photometric data points for each object to constrain the SED. Since the extensive photometry of our clusters covers a much wider wavelength range than G102 alone, this significantly improves the accuracy in modelling galaxy SEDs and correctly identifying spectral features.

We show two examples of cluster members with successful grism spectra and fits from grizli in Figure 3.1. The spectra of Object 407 shows a clear 4000Å break, while Object 288 has an [OII] line. We also show the corresponding grism redshift probabilities. Notably, Object 288 has a difference of only 0.002 between z_{spec} and z_{grism}, while Object 407 had no spectroscopic redshift measurements prior to grism reduction.

There are a number of reasons why grizli may fail to fit a spectrum. Some objects are too faint to produce a reliable trace on the grism image; some spectra may be cut off by the edge of the field of view; or some areas of the cluster may simply be too dense to obtain an uncontaminated spectrum. We also acknowledge that due to the nature of grism observations, the field of view includes spectra of foreground and background objects which do not belong to the cluster and lie at different redshifts. In this case, the observed wavelengths covered by the G102 grism may not cover any significant spectral features from that object. We note that this final case should not impact our objects of interest.

We assess each fit to ensure the redshift estimates are reliable. Firstly, we match the grizli object catalog with objects in our cluster catalogs, so that we only assess the grism spectra of known objects. We eliminate all objects from our grism sample for which grizli did not produce a fit with the inclusion of photometric data points. We then collect the z_{phot}, z_{grism}, and potential z_{spec} of each object. If none of the three redshift estimates lie within the range of the cluster or neighbour cut, we eliminate the object from our grism sample. If at least one redshift estimate lies within range of the cluster, we keep the object in the grism sample for assessment.

Secondly, we assess the reliability of the grizli fit of each remaining object by visually

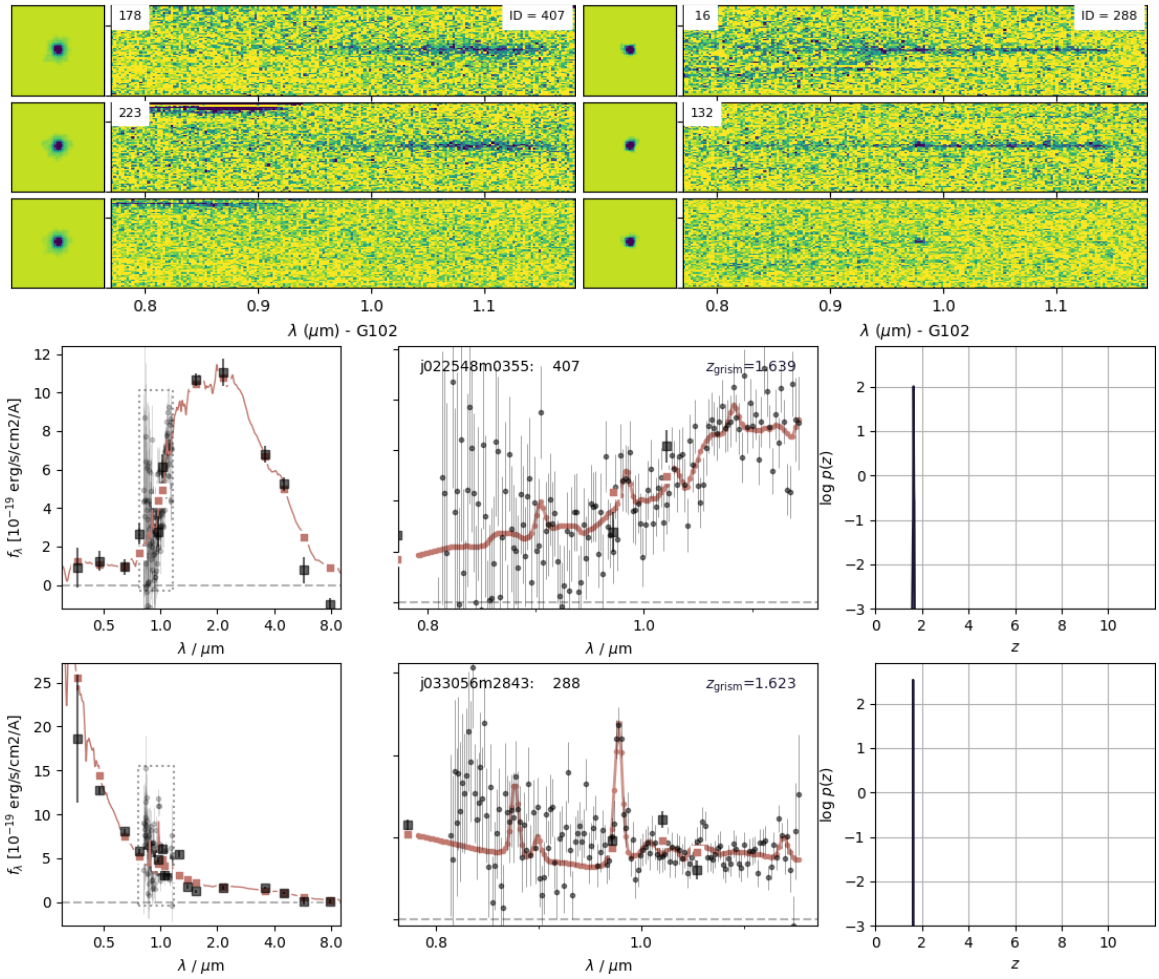

Figure 3.1: Examples of G102 grism spectra and successful fits of two cluster objects. The top panels of the figure are the 2D grism spectra of each object in two different position angles, followed by the residual after subtracting the contamination and continuum models. The bottom panels are the grizli output products for each object, including an SED fit with photometry, 1D spectrum, and grism redshift probability. Photometric points are shown as black squares.

inspecting the galaxy SED, 1D grism spectrum, and 2D grism spectrum. We note that even if a grism spectrum is faint or partially contaminated, grizli may be able to successfully fit an SED if the object has good photometry. We flag the grism redshift as unreliable for objects whose spectrum appears poorly resolved or does not include visible features such as a 4000Å break or [OII] emission line, as well as for objects whose spectral trace appears unreliable or badly contaminated. Contamination can sometimes be misread as an emission line in the 1D spectrum, which is why it is imperative to check all three data products. After assessment, the reliable grism redshifts are incorporated into our cluster catalog and used to help determine the best redshift of each galaxy.

3.1.2 Determining best redshift estimate

For each object in our cluster sample, we determine the best redshift estimate in order of measurement accuracy. Galaxy redshift estimates are used for two purposes: determining cluster/field membership (as in Section 2.3), and calculating projected local density. Since the range of cluster redshift determination is often much smaller than typical photometric redshift errors, it is important to obtain the most accurate redshifts we can for each galaxy.

We prioritize z_{spec} as the best redshift estimate for all objects that have spectroscopic redshift estimates. For a handful of cluster objects with both z_{spec} and reliable z_{grism}, we cross-reference z_{spec} to the spectroscopic catalog when there are large discrepancies compared to z_{grism} and z_{phot}. This very rarely results in z_{grism} being chosen over z_{spec}, when the origin of z_{spec} listed in the photometric catalog cannot be confirmed or z_{spec} conflicts with the MOSFIRE or FORS2 redshift measurement. As a simple general rule in these questionable cases, we choose to use z_{grism} as we are able to directly confirm the origin and quality of the measurement. We also use z_{grism} as the best redshift estimate for objects that have successful and reliable grizli fits and no z_{spec}. For objects with neither z_{spec} nor reliable z_{grism}, we use z_{phot} as the best redshift estimate.

Depending on which redshift type is determined to be the best estimate, we use equation 2.2, 2.3, or 2.4 to determine cluster membership. We find a total of 120 cluster members between our three clusters, including 42 based on z_{spec}, 17 based on z_{grism}, and 61 based on z_{phot}. The selection of field members is described in Section 2.3.3. We find a total of 642

Cluster	z_{spec} **members**	z_{grism} **members**	z_{phot} **members**	**Total**
CDFS44	5	6	31	42 (41)
XMM105	13	5	16	34 (28)
XMM113	24	6	14	44 (39)
Field	z_{spec} **galaxies**	z_{grism} **galaxies**	z_{phot} **galaxies**	**Total**
COSMOS	0	126	220	346 (258)
GOODS-S	15	134	147	296 (194)

Table 3.1: All members detected in F160W in each cluster and field, based on best redshift estimate. Numbers in brackets are the number of galaxies with successful morphological fits, as discussed in Section 3.2.3 for cluster members and Section 2.2.2 for field galaxies.

field members, including 15 based on z_{spec}, 260 based on z_{grism}, and 367 based on z_{phot}. The breakdown of cluster members and field galaxies is shown in Table 3.1.

For all galaxies, regardless of membership status, we keep the best redshift estimate for use in calculating projected local density.

3.2 Quantitative morphologies

3.2.1 Sérsic profiles

As mentioned in Chapter 1, fitting 2D Sérsic profiles is one method by which we can quantitatively measure galaxy morphology. A Sérsic profile expresses the intensity of light, I, as a function of radial distance from the center of an object, R. It can be expressed by the following equation:

$$I(R) = I_e \exp\left\{-b_n\left[\left(\frac{R}{R_e}\right)^{1/n} - 1\right]\right\} \tag{3.1}$$

where n is the Sérsic index, b_n is a function of n such that R_e is the radius at which half of the total light is contained, and I_e is the intensity of light at R_e. In two dimensions, Sérsic profiles are fit as an ellipse and parameterized by the ratio of semi-minor to semi-major axis (b/a) and the position angle of the object.

The Sérsic index effectively describes how centrally-peaked the light profile of an object is. High values of n indicate strong central peaks in the light profile, while lower values of n indicate flatter light profiles. Due to the different light profiles associated with typical elliptical and spiral morphologies, this makes the Sérsic index particularly useful as a quantitative morphology measurement. While typical values of the Sérsic index are found to change with cosmic time, particularly for high-mass quiescent galaxies, studies such as Buitrago et al. (2013) show that a delineation at $n = 2.5$ decently separates disk-dominated morphologies from bulge-dominated ones up to $z \sim 2.5$.

Going forward, we quantify the morphology of each galaxy in our sample by its Sérsic index, n. Building on examples set by previous work for $z \gtrsim 1$ (e.g. Matharu et al. 2019, van der Wel et al. 2014, and particularly Strazzullo et al. 2023), we define galaxies with $n < 1.5$ as disk-like, galaxies with $n > 2.5$ as bulge-like, and galaxies with $1.5 < n < 2.5$ as intermediate. We note that intermediate classification does not necessarily represent a unique morphological class, but does aid in reducing contamination between the disk-like and bulge-like classifications.

3.2.2 Finding PSFs

Fitting algorithms (such as GALFIT) rely on image convolution to model galaxies using a point-spread function (PSF), which contains information on how light spreads across pixels in an image. Nearby stars often appear among the brightest objects in many observational images, yet are small enough that they act as effective point-sources. One can therefore use cutouts of clean, non-saturated stars directly from the science image as empirical PSFs when modeling galaxy light profiles.

Prior to searching for PSFs, we perform source detection on the F160W images of our clusters using Source Extractor (Bertin & Arnouts 1996). We use parameters from the output catalog to locate suitable stars, assist in making object cutouts, and set initial parameters necessary to model Sérsic fits. We additionally use Source Extractor to create a segmentation map which we use for object masking.

Following Matharu et al. (2019), we select PSF candidates from objects with $15 <$ MAG_AUTO < 19. These limits are chosen to exclude oversaturated stars and ensure

that the PSF is not too faint, both of which can reduce the quality and impact the results of the galaxy models. CLASS_STAR estimates of the likelihood that an object is a point source from 0 to 1. While it is not a perfect estimate, we use this as a secondary parameter to ensure that our selection is not contaminated bright galaxies, by requiring all PSF candidates to have CLASS_STAR > 0.5. Even without placing selection limits on the radius of our PSF candidates, we find that our magnitude selection is bright enough to select objects with typical values of FLUX_RADIUS ≈ 2.5 and CLASS_STAR > 0.8, showing that this range is, on-average, well-suited to selecting stars.

We create cutouts of each PSF candidate and visually assess them to ensure they are centered on star-like objects. We also check for PSF candidates which appear dim or contaminated by background objects. We find four PSF candidates in CDFS44. We find three PSF candidates in XMM105, one of which we remove due to contamination directly overlapping a diffraction spike. We encounter a problem with our PSF search in cluster XMM113, where we detect only a single PSF candidate within our initial selection limits. This candidate is very close to our bright magnitude limit with MAG_AUTO = 15.20, and visual inspection shows it is likely an oversaturated star with diffraction spikes that extend beyond the boundaries of the 100×100 pixel cutout image.

We examine the distribution of MAG_AUTO vs FLUX_RADIUS for objects in XMM113 and repeat our search by extending to dimmer magnitudes and lower CLASS_STAR values. We find an additional three PSF candidates: one star with MAG_AUTO = 19.76, and two faint stars with MAG_AUTO = 21.06 and 20.55 respectively. While brighter, the MAG_AUTO = 19.76 star unfortunately lies too close to a background galaxy to easily mask out, so we chose to eliminate it from our PSF candidates. Instead, we create a new PSF by stacking the two faintest stars, utilizing the segmentation map to mask out contamination prior to stacking. Cutouts of the four PSF candidates in XMM113 are shown in Figure 3.2, alongside the contamination masking and final stacked PSF.

Finally, we test fit a sample galaxy from each cluster to ensure consistency between our PSFs. We use GALFIT to fit a single-component Sérsic profile to a galaxy with fixed input parameters using each available PSF. We compare the output parameters as well as visually assess the models and residuals to look for any significant differences among the PSFs. In the case of XMM113, where we do not have multiple usable PSFs, we instead compare

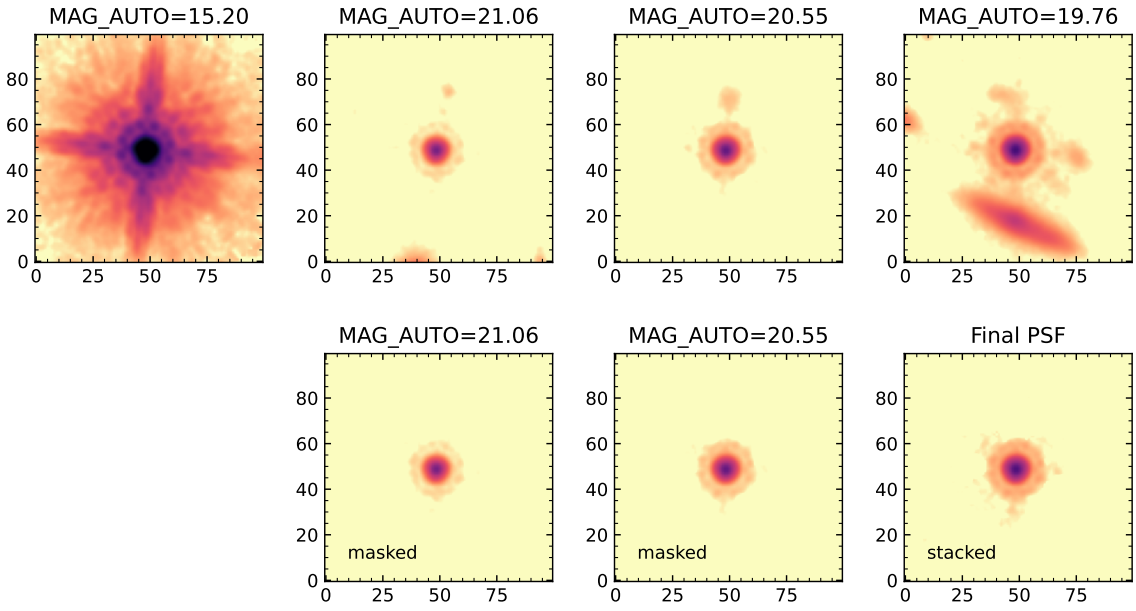

Figure 3.2: The four PSF candidates for cluster XMM113, including Source Extractor magnitudes. Top row shows the original image cutouts. Bottom row shows the two faintest PSF candidates with contamination masked out, as well as the final PSF made by stacking the two masked cutouts.

the fits between multiple cluster galaxies using the oversaturated PSF candidate and our stacked PSF. As expected, the oversaturated PSF candidate does a poor job of modeling many galaxies, leaving prominent outer rings in the residuals of multiple fits. Meanwhile, our stacked PSF seems to adequately model galaxies with no significant features left in the residuals. We therefore continue our analysis with the chosen PSFs in CDFS44 and XMM105, and the stacked PSF in XMM113.

3.2.3 Fitting light profiles with GALFIT

We fit our cluster members to single-component Sérsic profiles using GALFIT (Peng et al. 2002, 2010a). GALFIT is an algorithm designed to fit the 2D light profiles of galaxies to analytical models using χ^2 statistics. It allows the user choice of multiple function types, as well as simultaneous fitting of multiple components and multiple objects within a single image. In order to automatically fit batches of images, we use a Python-based GALIFT wrapper designed by Matharu et al. (2019). The wrapper uses a two-stage iterative process to prevent GALFIT from becoming stuck on a "local minimum" fit, and has been shown to

produce results in good agreement with the Sérsic fits of van der Wel et al. (2012). Additionally, rather than leaving GALFIT to estimate the noise in each image cutout, we create sigma images for each cluster out of the weight maps, following $\sigma = 1/\sqrt{weight}$.

The first stage of our GALFIT process involves making a first attempt at a light profile fit to our galaxies. We use the output Source Extractor parameters as initial guesses for the integrated magnitude, R_e, axis ratio, and position angle of each object. We also set an initial guess of $n = 2.5$ for each object, which is required by GALFIT. We create image cutouts centered on the primary galaxy to be fit, with an initial cutout size of 10 × FLUX_RAD, with a minimum size of 40 pixels and a maximum size of 400 pixels. We have GALFIT simultaneously fit all objects with MAG_AUTO < 26 whose centers lie inside the cutout image. We use the segmentation map to mask out all objects that are not included in the simultaneous fitting. We find that masking is a more efficient method of dealing with objects that are too faint or extended objects whose centers lay outside the cutout image, as GALFIT frequently has trouble modelling these objects accurately or attempts to account for their light in the fit of another object. In the first attempt, we also use constraint files to ensure that GALFIT sticks to realistic values for galaxy parameters and fits the intended object. Among the constraints, we limit the Sérsic index to $0.3 \leq n \leq 8$, following van der Wel et al. (2012). Inclusion of both the constraint files and masking significantly improves the chance to converge on a solution instead of crashing.

The results of the first fit are then used initial guesses for the second GALFIT run. We extend our image cutouts to 15 × FLUX_RAD, and set new initial guesses for the primary object's axis ratio and position angle from the output of the first fit, keeping the initial values for other parameters unchanged. We simultaneously fit secondary objects within the cutout in the same way as the first fit. If a secondary object was fit independently as a primary galaxy, we use the values found from its primary fit as new initial parameters. If it was not, we again use the Source Extractor values. As in the first fit, we mask out all other objects for the new cutouts. We do not use constraint files in the second fit, and instead allow all objects to be fit freely.

We show examples of the second fits from each cluster in Figure 3.3. For each galaxy, we include the final n and R_e values, and show the image cutout, Sérsic model, and the residual (model subtracted from the cutout). At the resolution of our images, most galaxies

in our clusters are well-fit with a single Sérsic profile—however, we note that there are a few galaxies where the residuals still display a sharp peak in the very center and/or a thin ring around the core. We do not comment on the origin of these features, nor do we attempt to modify our fits to specifically accommodate this small subgroup of objects.

We remove any galaxies from our cluster member sample for which GALFIT failed to converge on a second fit, but keep them as potential neighbours for calculating local density. This removes exactly 10 percent of our redshift-selected F160W cluster members overall. XMM105 is the most strongly impacted with 15.8 percent (6 galaxies) removed. The number of galaxies remaining are shown in brackets in the Total column of Table 3.1.

3.3 Local density

3.3.1 *N*th-Nearest Neighbours

We follow the convention set by previous major studies and calculate local galaxy density using the *N*th-Nearest Neighbours method. The method is fairly simple in concept, but has proven to be surprisingly robust across decades of studies. Postman et al. (2005) perform a comparison between *N*th-Nearest Neighbours and the Friends-of-Friends algorithm (FoF) for calculating local density, ultimately finding that the trends of their morphology-density relation do not change with choice of method. Their results indicate that the simpler *N*th-Nearest Neighbours approach is equally suited to recovering local density estimates as FoF. We further direct the reader to Cooper et al. (2005) for an assessment of various methods of measuring local density at $z \gtrsim 1$.

*N*th-Nearest Neighbours calculates the unique local density of any galaxy by using the area (or volume) containing the galaxy and its *N* nearest neighbouring galaxies. In practice, if one knows the position of all objects in a sample, they can calculate the local density for any individual object. The calculation of *N*th-Nearest Neighbours requires no prior assumptions about the galaxy distribution, and is particularly advantageous for our study as it can be used in any environment. In other words, *N*th-Nearest Neighbours can be applied to low-density field galaxies as well as high-density cluster galaxies.

The choice of *N* is one of the few direct variables in this method. Dressler (1980) and

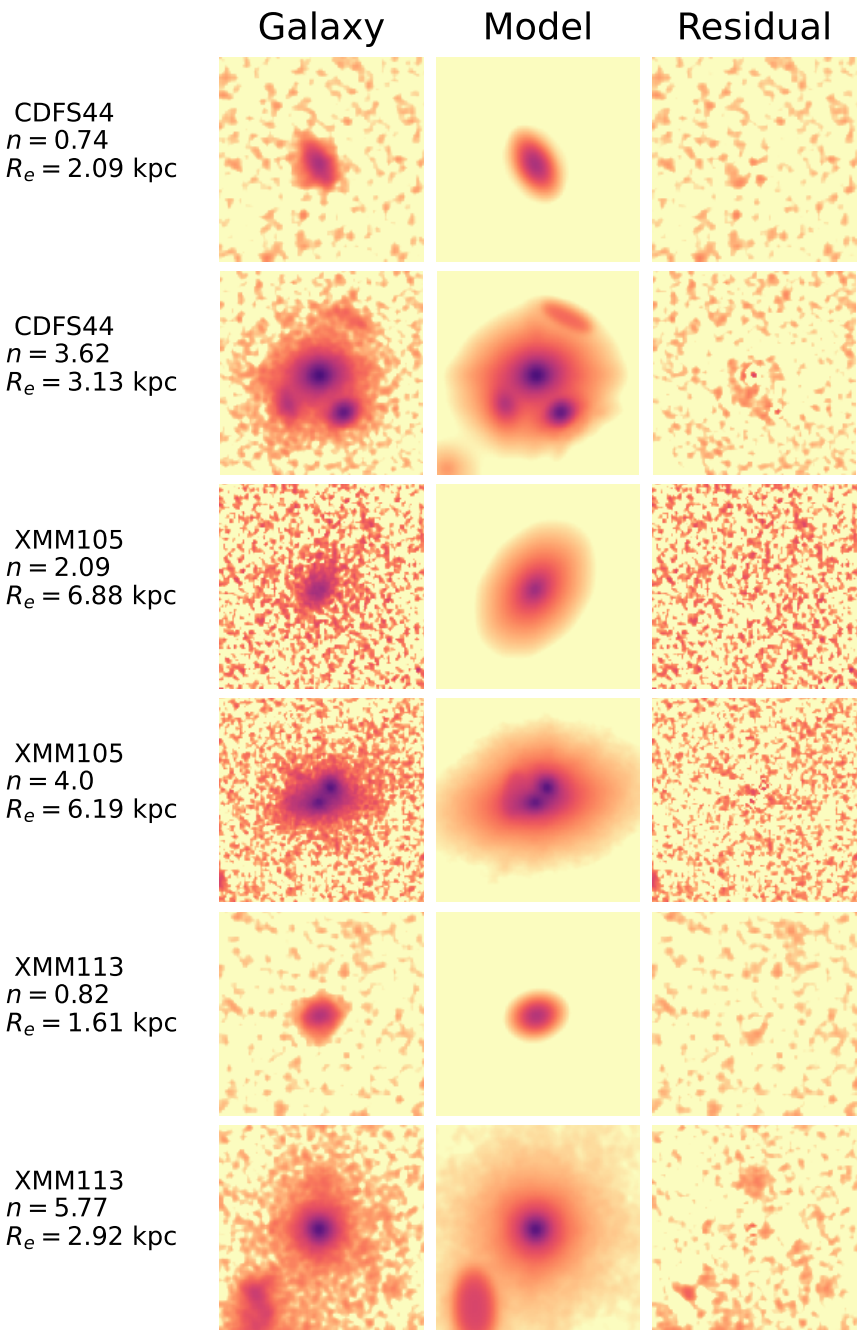

Figure 3.3: Examples of cluster galaxies fit to single-component Sérsic profiles with GALFIT. The Sérsic index, n, and effective radius, R_e, of the central galaxy in each cutout are given on the left. From left to right, the columns show the original galaxy cutout in F160W, the GALFIT model of all objects within the cutout, and the residual (cutout minus model). Two galaxies from each cluster were chosen to span a range of n.

Dressler et al. (1997) use $N = 10$ for their studies of galaxies at $z \sim 0$ and $z \sim 0.5$, while Postman et al. (2005) use $N = 7$ for galaxies at $z \sim 1$. Many observational papers have noted that their choice of N within $\pm$ 2-3 does not significantly influence their results (e.g. Postman et al. 2005; Bluck et al. 2019). This result is echoed by Cooper et al. (2005), who conclude that while increasing N ultimately smooths the density distribution, low-density environments are relatively insensitive to small choices of N, while high-density environments are not likely to be sensitive to N so long as it is smaller than the overall richness of the cluster under consideration.

We proceed in our analysis with $N = 5$, which is chosen mainly to account for the fewer number of cluster members detected at $z \sim 1.6$ compared to low-z clusters. We also note that we will be calculating the local densities of both cluster and field galaxies in an identical manner, allowing us to make direct comparisons between cluster and field environments. Goto et al. (2003) use the same method to calculate the local density of low redshift galaxies in SDSS, which enables them to perform an analysis of the full data set with no distinction between cluster and field galaxies.

3.3.2 Projected 2D galaxy densities

We calculate projected 2D galaxy densities following the methods outlined in Cooper et al. (2005). While Cooper et al. (2005) include a methodology for calculating 3D densities, we note that projected densities are less sensitive to uncertainties in line-of-sight velocity/redshift estimates. Given that our sample still includes many galaxies with only photometric redshift estimates, using 2D projected densities will ensure more robust measurements for our sample overall.

Following the method described in Cooper et al. (2005)—also notably used in Goto et al. (2003)—we eliminate foreground and background interlopers from influencing density calculations by locating projected neighbours within limited slices in line-of-sight velocity/redshift space. Many other studies, including Dressler (1980), Dressler et al. (1997), and Postman et al. (2005), use statistical background subtraction to correct their morphological fractions using an estimate of the possible contamination from field galaxies. We consider our method to be more accurate, although we acknowledge that it is only possible

due to our sample's extensive photometric coverage, allowing us to use photometric redshift estimates for galaxies which lack spectroscopic and grism redshifts.

We develop our own independent Python code for calculating the local density of galaxies in our sample. This allows us to have full control over the method and its implementation, including the value N, choice of projected vs. 3D densities, line-of-sight velocity slices, and distance calculations.

As defined in Cooper et al. (2005), we use the following equation to calculate the projected local galaxy density of a galaxy, Σ_N, in a circular area:

$$\Sigma_N = \frac{N}{\pi D_N^2} \tag{3.2}$$

where we set $N = 5$, and therefore $D_N = D_5$, the projected distance to the galaxy's 5th nearest neighbour in Mpc.

For each cluster or field member, we locate all neighbouring galaxies within $\pm$3000 km s^{-1} line-of-sight velocity, calculated using the best redshift estimate for each galaxy as described in Section 3.1.2. At $z = 1.6$, this is equivalent to a redshift range of $\pm$0.026. We calculate the projected 2D distance to each neighbour in angular sky coordinates first, and then convert to proper Mpc based on the redshift of the primary member galaxy. Neighbours are sorted by increasing distance, and finally Σ_5 is calculated using equation 3.2.

3.3.3 Edge effects

Edge effects can occur when a galaxy is closer to the edge of the detection image ($D_{\rm edge}$) than it is to its Nth neighbour (D_N). In such a case, it cannot be known whether an undetected neighbour exists beyond the bounds of the image that is closer to the edge galaxy than the observed D_N. This introduces a new source of uncertainty in local density measurements. There are multiple ways to handle the uncertainty from edge effects, including: selecting for members within a minimum distance from the image edge; removing edge galaxies from the sample entirely (Poggianti et al. 2008); reducing N for edge galaxies such that $D_N \leq D_{\rm edge}$ (van der Wel et al. 2007); treating D_N as an upper limit and $D_{\rm edge}$ as a lower limit for edge galaxies (or other limiting methods such as Baldry et al. 2006); or adjusting the area used in density calculations (Goto et al. 2003; Bamford et al. 2009; Tasca et al. 2009).

The mixed of ground-based and *HST* imaging of our clusters imposes a more complicated scenario in our consideration of edge effects. If we consider only the galaxies detected within the F160W field of view, our cluster members are certainly impacted by edge effects. However, our cluster catalogs also contain many galaxies which were detected in ground-based observations, covering a larger sky area beyond the bounds of the F160W field of view. As a simpler alternative to direct corrections methods of handling edge effects, such as those recommended above, we include these galaxies outside the F160W field of view in our potential neighbour sample, hoping to "catch" the undetected neighbours. This is somewhat similar to the method of Huertas-Company et al. (2009), who mitigate edge effects by extending the area in which they search for neighbours.

We acknowledge that this method is not perfect, and its accuracy depends on whether the ground-based observations have detected a sample of neighbour galaxies functionally equivalent to those detected within F160W (i.e. similar completeness). Additionally, we have applied no corrections for edge effects to the field. For the purposes of this study, we will assume that the sky coverage of the fields is large enough that edge galaxies do not significantly impact our results. Ideally, future work should include proper and equitable treatment of edge effects across all samples.

Chapter 4

Results

4.1 The size-mass relation

We plot the size-stellar mass relation for cluster and field members in Figure 4.1, using R_e as measured from the Sérsic fits. Star-forming and quiescent galaxies are selected by UVJ cutoff (as described in Williams et al. 2009), shown as pale blue circles and orange diamonds respectively. As comparison, we also plot the trends from van der Wel et al. (2014) for $z = 1.25$ (dotted lines) and $z = 1.75$ (dashed lines) for both early-type (red) and late-type galaxies (violet). As van der Wel et al. (2014) define their early-type and late-type galaxies using UVJ selection, this is equivalent to our selection of star-forming and quiescent galaxies.

Both cluster and field star-forming galaxies follow the expected trends in the size-mass relation. While star-forming galaxies show a fair amount of scatter on both sides of the trendline, quiescent galaxies in both environments have a larger scatter above the trendline than below it. This is not unexpected, as previous studies of the size-mass relation at various redshifts also show that quiescent galazies have a larger scatter above the trendline (for example, see Figure 5 in van der Wel et al. 2014 and Figure 7 in Matharu et al. 2019).

At $z \sim 1$, Matharu et al. (2019) find that cluster galaxies are systematically smaller than field galaxies by approximately -0.07 and -0.08 dex for star-forming and quiescent galaxies respectively. We cannot comment on specific agreement or disagreement in this regard, as calculations of this type would require careful weighting of each galaxy to determine the

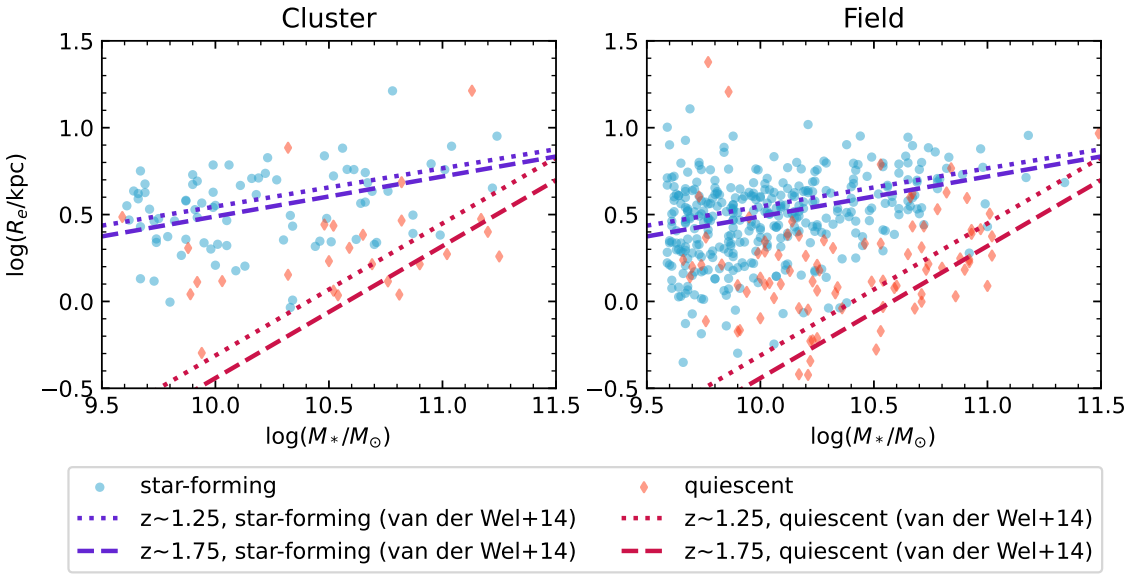

Figure 4.1: Size-stellar mass relation at $z \sim 1.6$ for cluster and field members. UVJ-selected star-forming and quiescent galaxies are shown as pale blue circles and orange diamonds, respectively. Trends from van der Wel et al. (2014) are plotted for $z = 1.25$ (dotted lines) and $z = 1.75$ (dashed lines) early-type (red) and late-type galaxies (violet).

unique trendlines of our sample. While this may be possible with for the field members, we note that we have a sparse number of quiescent galaxies among our cluster members, which would make any fits to these galaxies highly uncertain. This is in part due to a smaller sample size of clusters than in Matharu et al. (2019), however, Nantais et al. (2017) also find that our three $z \sim 1.6$ clusters have a much lower fraction of UVJ-selected quiescent galaxies than clusters at lower redshift. The uncertainties due to our small number of quiescent cluster galaxies would dwarf the statistical differences found by Matharu et al. (2019), and greatly impact any comparison between cluster and field. However, our results do suggest very little difference between the overall sizes of cluster and field galaxies, which is roughly consistent with the small differences found by Matharu et al. (2019).

Aside from our small number of quiescent cluster galaxies, our size-mass relation appears to be in good agreement with other studies at $z \sim 1.6$, such as Strazzullo et al. (2023).

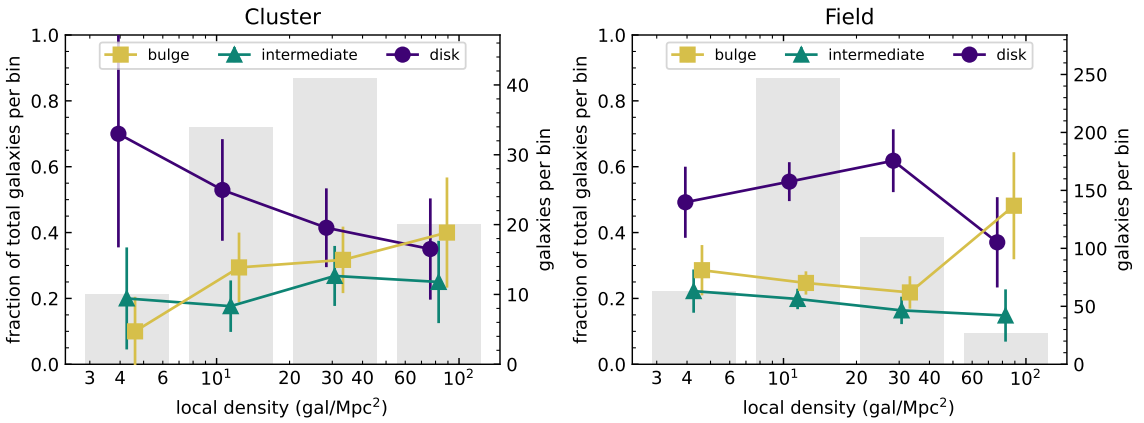

Figure 4.2: The morphology-density relation at $z \sim 1.6$ in clusters and the field, plotted in 4 bins of projected local density, Σ_5. The total number of galaxies in each bin is underplotted as a grey histogram, following the right-hand y-axis. Error bars are given by Poisson statistics.

4.2 The morphology-density relation

For ease of discussion, we will refer to our disk-like and bulge-like classifications as simply "disk" and "bulge" throughout the remainder of this chapter.

In Figure 4.2, we plot the morphological fractions of cluster and field members in bins of local density. Disk galaxies ($n < 1.5$) are plotted as purple circles, intermediate galaxies ($1.5 < n < 2.5$) are plotted as green triangles, and bulge galaxies ($n > 2.5$) are plotted as yellow squares. Each morphological type is plotted offset from the bin centers for clarity. Bin sizes are logarithmic in local density and chosen to simultaneously balance the number of galaxies in each bin for both cluster and field samples. We underplot the number of galaxies in each density bin as a grey histogram, as shown on the right-hand y-axis. Error bars are given by Poisson statistics, where the uncertainty from the number of galaxies of each morphological type is added in quadrature with the uncertainty in the total galaxies per bin.

We note that the cluster fractions in the low-density end and field fractions in the high-density end are more sensitive to bin numbers and sizes due to small sample numbers. Our bins were chosen such that the lowest density bin, centered on $\Sigma_5 = 4.26$ gal/Mpc^2, contains a minimum of 10 cluster galaxies (9.5 percent of the cluster members within the plot

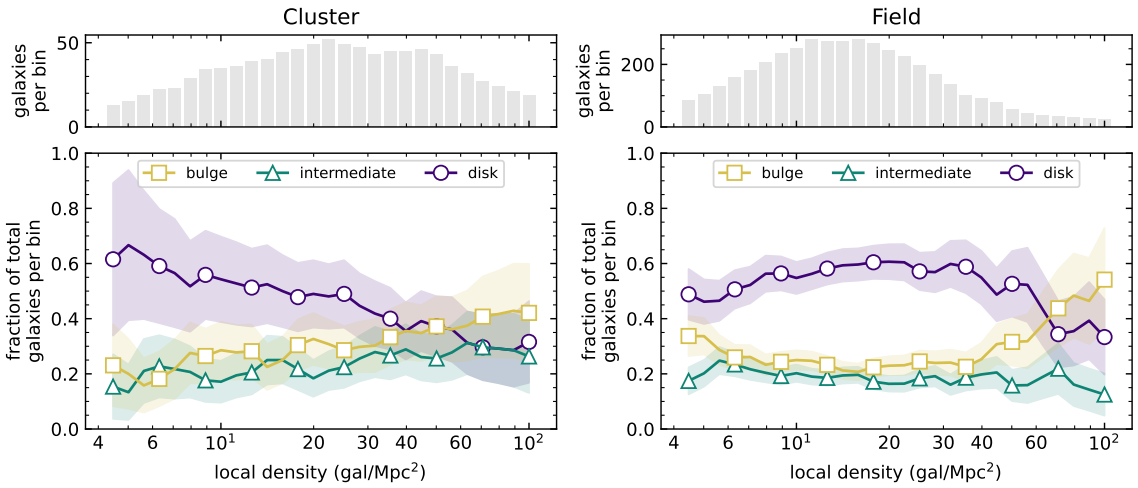

Figure 4.3: The morphology-density relation at $z \sim 1.6$ in clusters and the field, plotted using a fixed-width box kernel. The total number of galaxies per bin is plotted as a grey histogram in the panel above each relation. Shaded regions represent errors given by Poisson statistics. Markers are placed every 3 points to help guide the eye. Details of the box kernel width and spacing are given in the text.

boundaries). Meanwhile, the highest density bin, centered on $\Sigma_5 = 82.4$ gal/Mpc^2, contains 27 field galaxies (roughly 6 percent of the field members within the plot boundaries). This is expected due to the natural density distributions of the two samples, and is our biggest consideration when attempting to compare results directly between both environments. However, this sensitivity to bin choice adds additional restrictions to classic binning methods, and limits our ability to examine either trend in detail.

To mitigate this, we plot the morphology-density relation using a fixed-width box kernel in Figure 4.3. This has the benefit of making our results less sensitive to specific binning choices, while also allowing us to extrapolate more detail with the same sample sizes. The box kernel is constructed with bin sizes of $\pm 0.25 \log(\Sigma_5)$ and a spacing of $0.05 \log(\Sigma_5)$ between bin centers. The total number of galaxies per bin is plotted as a grey histogram in the panel above each relation. Note that the histograms do not represent the true bin widths, as box kernel bins are not fully independent. Errors are calculated in the same way as in Figure 4.2, shown here as shaded areas above and below the trend. Markers are placed every 3 points to help guide the eye.

We find a clear trend of morphology with density in our $z \sim 1.6$ clusters. At low densities ($\Sigma_5 \approx 4.47$ gal/Mpc^2) disk galaxies make up approximately 60 ± 20 percent of the cluster population, intermediate galaxies approximately 20 ± 10 percent, and bulge galaxies approximately 20 ± 10 percent. The cluster trends smoothly such that at high densities ($\Sigma_5 \approx 100$ gal/Mpc^2), the disk fraction decreases to approximately 30 ± 10 percent, the intermediate fraction increases slightly to 30 ± 10 percent, and the bulge fraction increases to approximately 40 ± 20 percent.

Meanwhile, the field fractions differ from clusters slightly at low density, showing a slight shortage of disks at 49 ± 9 percent, a similar amount of intermediates at 17 ± 5 percent, and an excess of bulges at 34 ± 7 percent. Moderate-density field fractions, however, look fairly flat with values similar to the low-density cluster fractions. For example, at $\Sigma_5 = 35.5$ gal/Mpc^2, the field is 60 ± 10 percent disks, 19 ± 5 percent intermediates, and 22 ± 5 percent bulges. At high densities, the field fractions change steeply. In the highest density bin ($\Sigma_5 \approx 100$ gal/Mpc^2), the field fractions reach 30 ± 10 percent disks, 12 ± 8 percent intermediates, and 50 ± 20 percent bulges.

We comment again that it should be extremely uncommon for field galaxies to reside in densities similar to cluster centers. This is echoed in the decline of the number of field galaxies per bin with increasing local density. Although we report the high-density field results here, we are careful not to over-interpret these trends. While it is possible that some or all of the high-density field galaxies may reside within small compact groups, some may also be errors due to projection effects. We will explicitly refrain from interpreting the trends above $\Sigma_5 \gtrsim 40$ gal/Mpc^2 as representative of the global field environment.

To facilitate a more direct measurement and comparison of the strength of the morphology-density relation, we fit simple linear trendlines to each morphological fraction in both cluster and field environments in Figure 4.4. We use linear regression to find the best-fit line of each morphological fraction as a function of $\log(\Sigma_5)$, weighting each bin by its associated error. Cluster (red) and field fractions (cyan) are plotted on top of each other for each morphological type. The best fit to the cluster fractions is plotted as a solid red line, while the best fit to the cluster fractions is plotted as a dashed cyan line.

The parameters for each best fit line are given in Table 4.1 with errors. For all morphological types, we find that the slope of the best-fit line with density is steeper in the cluster

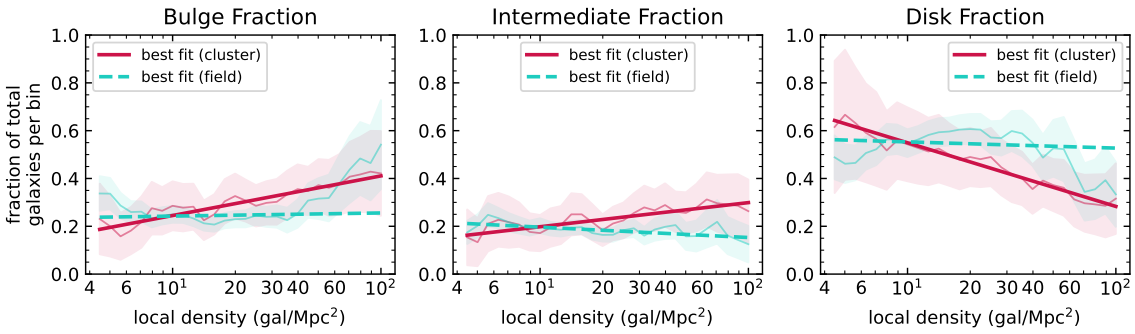

Figure 4.4: The fractions of each morphological type with local density (Σ_5) are compared directly between cluster (red) and field members (cyan) at $z \sim 1.6$. Linear regression has been used to find the best fit line to each fraction as a function of $\log(\Sigma_5)$, which is plotted for the cluster (solid red line) and field environments (dashed cyan line).

	Cluster		**Field**	
Fraction	**Slope**	**Intercept**	**Slope**	**Intercept**
Bulge	0.17 ± 0.02	0.08 ± 0.02	0.01 ± 0.03	0.23 ± 0.03
Intermediate	0.10 ± 0.01	0.10 ± 0.02	-0.04 ± 0.01	0.24 ± 0.01
Disk	-0.27 ± 0.01	0.82 ± 0.02	-0.03 ± 0.04	0.58 ± 0.05

Table 4.1: Linear regression parameters for the best fit line to each morphological fraction in the morphology-density relation, as plotted in Fig. 4.4. Morphological fractions are given as a function of $\log(\Sigma_5)$.

environment than the field. All three cluster trends are well-fit by a straight line within the local density range of Figure 4.4. Within the same range in the field, linear regression does a reasonable job at tracing the trends at moderate densities, but provides a poor fit to the high-density end. We refer the reader to our earlier comments about high-density field galaxies, and thus we do not over-analyze this result.

We conclude that the morphology-density relation is in place in our $z \sim 1.6$ clusters, resulting in the fraction of disk galaxies decreasing with local density while the fraction of bulge galaxies increases. We do not find conclusive evidence of a similar relationship between morphology and local density across the majority of the field environment.

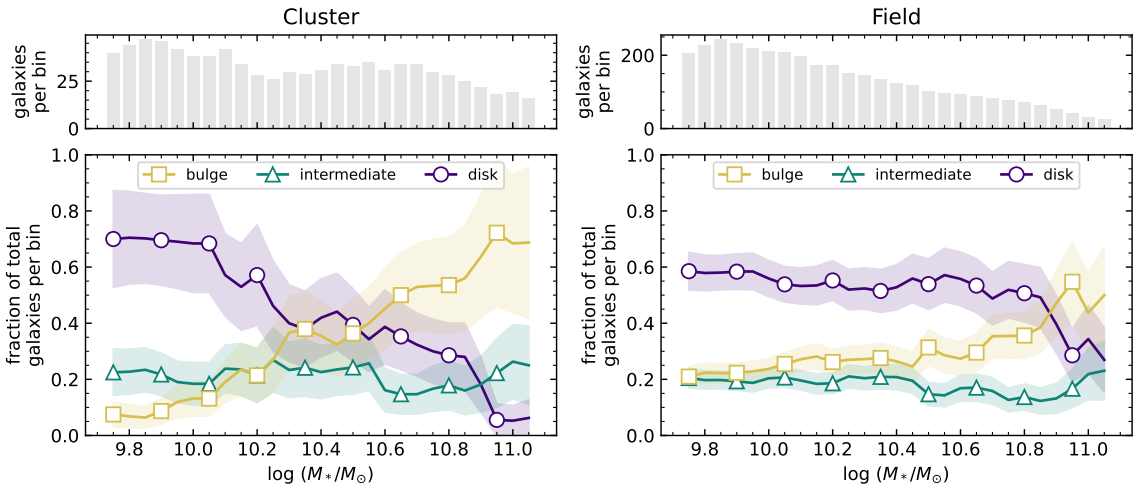

Figure 4.5: The morphology-stellar mass relation at $z \sim 1.6$ in clusters and the field, plotted using a fixed-width box kernel. The total number of galaxies per bin is plotted as a grey histogram in the panel above each relation. Shaded regions represent errors given by Poisson statistics. Markers are placed every 3 points to help guide the eye. Details of the box kernel width and spacing are given in the text.

4.3 The morphology-mass relation

We next turn our attention to the relationship between morphology and stellar mass, which may elucidate the role of intrinsic morphological evolution. In Figure 4.5, we plot the morphology-stellar mass relation in both cluster and field environments. We use the same box kernel method as in Figure 4.3, replacing $\log(\Sigma_5)$ with $\log(M_*/M_\odot)$. Throughout this section, we use "low mass" as shorthand for $\log(M_*/M_\odot) \approx 9.75$ and "high mass" as shorthand for $\log(M_*/M_\odot) \approx 11.05$, since these are the bounds of our plots.

We find significant differences in the morphology-mass relationship between environments. Within clusters, the disk galaxy fraction decreases almost smoothly from 70 ± 20 percent at low masses to only 6 ± 6 percent at high masses. This is coupled with a proportional increase in the bulge galaxy fraction from 8 ± 4 percent at low masses to 70 ± 30 percent at high masses. Meanwhile, the intermediate fraction stays roughly the same at all stellar masses—22 ± 8 at low masses and 20 ± 10 percent at high masses.

The field morphology-mass relation appears quite different. At low masses, the fractions of bulge and intermediate galaxies are 21 ± 4 and 20 ± 3 percent respectively, while disk galaxies dominate at 59 ± 7 percent. Up to $\log(M_*/M_\odot) = 10.8$, the bulge galaxy fraction

	Cluster		Field	
Fraction	**Slope**	**Intercept**	**Slope**	**Intercept**
Bulge	0.48 ± 0.02	-4.7 ± 0.2	0.13 ± 0.02	-1.1 ± 0.2
Intermediate	-0.03 ± 0.02	0.6 ± 0.2	-0.05 ± 0.01	0.7 ± 0.1
Disk	-0.56 ± 0.03	6.2 ± 0.3	-0.14 ± 0.02	2.0 ± 0.2

Table 4.2: Linear regression parameters for the best fit line to each morphological fraction in the morphology-mass relation, as plotted in Fig. 4.6. Morphological fractions are given as a function of $\log(M_*/M_\odot)$. Intercept parameters are presented for completeness but are not representative of physical values.

increases slowly but steadily to 36 ± 8 percent, while the disk galaxy fraction decreases more slowly to 50 ± 10 percent. Between $10.8 < \log(M_*/M_\odot) \leq 11.05$, the bulge galaxy fraction increases more steeply to approximately 50 ± 20 percent, while the disk fraction steeply declines to 30 ± 10 percent at high masses. The intermediate fraction in the field remains roughly consistent with $15 - 20$ percent at all stellar masses, decreasing slightly to 14 ± 4 at $\log(M_*/M_\odot) = 10.8$, but returning to 20 ± 10 at high masses.

We note that in both cluster and field environments, the number of galaxies per bin peaks in the stellar mass bin centered at $\log(M_*/M_\odot) = 9.85$, and declines in the two less massive bins. This is an artefact of our choice of bin boundaries and stellar mass limit. Our first two stellar mass bins are $\log(M_*/M_\odot) = 9.75 \pm 0.25$ and $\log(M_*/M_\odot) = 9.80 \pm 0.25$, meaning that their low-end boundaries lay below our stellar mass completeness limit of $10^{9.58} M_\odot$. Decreasing in stellar mass from the 9.80 bin to the 9.75 bin, we are therefore losing galaxies from the upper boundary of the bin while gaining none from the lower boundary, resulting in a lower number of galaxies overall. We could remove these first two bins from our analysis, however, there is no significant change in the trends of cluster nor field galaxies in this range, and therefore the choice to include or exclude the two lowest-mass bins does not impact our results.

Following our analysis of the morphology-density relation in Section 4.2, we fit linear trendlines to each morphological fraction as a function stellar mass, shown in Figure 4.6. The details of the trendlines and plots are identical to that of Figure 4.4, with local density replaced by galaxy stellar mass. Parameters of each trendline are given in Table 4.2 with errors.

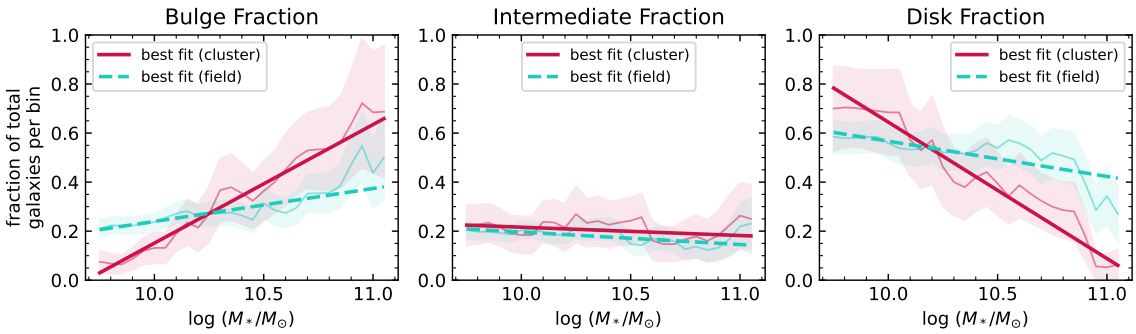

Figure 4.6: The fractions of each morphological type with stellar mass (M_*) are compared directly between cluster (red) and field members (cyan) at $z \sim 1.6$. Linear regression has been used to find the best fit line to each fraction as a function of $\log(M* /M_\odot)$, which has been plotted for the cluster (solid red line) and field environments (dashed cyan line).

The linear trendlines make it clear that in clusters, the fraction of bulge galaxies tends to zero at low stellar masses, while the fraction of disk galaxies tends to zero at high stellar masses. The trends of bulge and disk fractions are significantly different between the cluster and field environments, while the trends of intermediate galaxy fractions are virtually identical between the two environments. We note that, following the trends described earlier in this section, a single linear fit may not be accurate to each of the observed morphological trends in the field. We suggest that a non-linear or perhaps piecewise-linear trend about $\log(M_*/M_\odot) \approx 10.8$ may be a better fit to the morphology-mass relation in field galaxies. We show an example of a piecewise-linear fit in Appendix B, however, further analysis is beyond the scope of this thesis.

To summarize, we find a strong relationship between morphology and stellar mass in cluster galaxies, such that disk fractions strongly decrease and bulge fractions strongly increase for increasing stellar mass. The majority of field galaxies display a very weak relationship between morphology and stellar mass compared to cluster galaxies. However, we also find that the field relationship undergoes a significant change in slope around $\log(M_*/M_\odot) \approx 10.8$, such that the fraction of disk galaxies declines sharply above this stellar mass. This suggests that galaxy stellar mass is not a universally-strong indicator of galaxy morphology at $z \sim 1.6$. The comparison between our morphology-mass and morphology-density relations suggests that the environmental processes driving the morphology-density

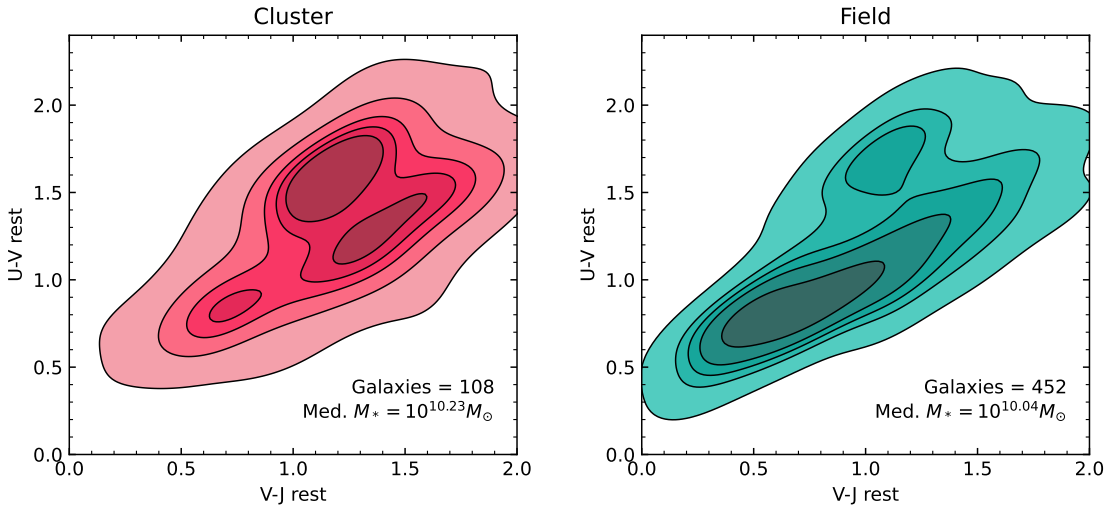

Figure 4.7: Rest-frame UVJ diagrams showing the overall distribution of cluster and field members at $z \sim 1.6$. Data is visualized using a 2D KDE plot such that curves represent areas of similar number density.

relation are mass-dependent. We discuss the potential physical processes driving these relations further in Section 5.3.

4.4 The effect of morphology and environment on galaxy colours

As our final piece of analysis, we explore the relationship between environment, morphology, and galaxy colour. In Figure 4.7, we use a UVJ diagram to plot the distributions of rest-frame galaxy colours for cluster and field members. We plot the data using a 2D kernel density estimate (KDE) rather than a traditional scatter plot to better visualize the colour regions where galaxies are most likely to reside. The total number of galaxies in each distribution are shown on the plots, along with the median stellar mass. While all galaxies lie above the stellar mass completeness limit, we note as a caveat that the stellar mass distributions of cluster and field galaxies are not identical.

Figure 4.7 shows the known relation that galaxies primarily occupy three regions of the UVJ diagram. While rest-frame $U - V$ colours separate red and blue galaxies (high and low $U - V$ colours respectively), the addition of $V - J$ allows us to separate red galaxies into

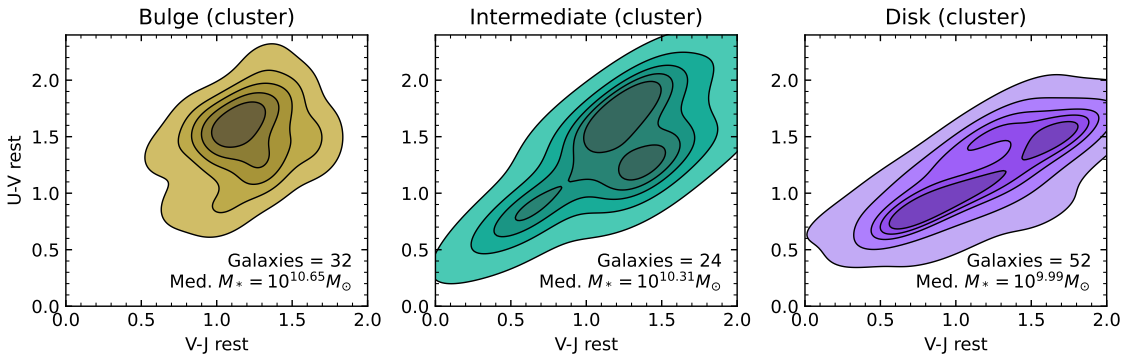

Figure 4.8: Rest-frame UVJ diagrams showing the distribution of $z \sim 1.6$ cluster galaxies separated by morphological type. Data is visualized as in Figure 4.7.

those that are quiescent/quenched of star formation (high $U - V$ and moderate $V - J$), and star-forming galaxies that are reddened by dust (high $U - V$ and high $V - J$). In a general sense, we find that galaxies in clusters are more likely to be quenched or dusty than those in the field at $z \sim 1.6$. Cluster galaxies also predominantly appear red overall, while field galaxies predominantly appear blue.

We break down our cluster and field galaxies into disk ($n < 1.5$), intermediate ($1.5 < n < 2.5$), and bulge morphologies ($n > 2,5$), and separately plot their UVJ diagrams. Cluster galaxies are shown in Figure 4.8 and field galaxies are shown in Figure 4.9.

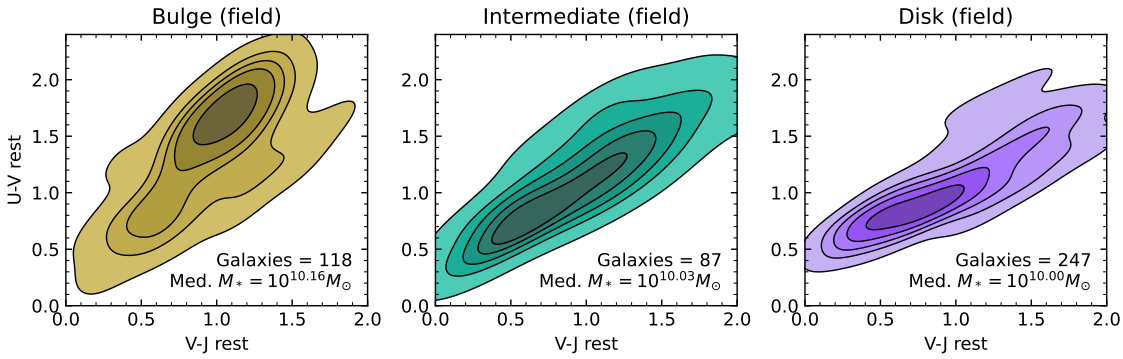

Figure 4.9: Rest-frame UVJ diagrams showing the distribution of $z \sim 1.6$ field galaxies separated by morphological type. Data is visualized as in Figure 4.7.

We find evidence for a higher fraction of dusty disk galaxies in clusters than in the field. While intermediate galaxies in the field are dominantly blue and star-forming, intermediate

galaxies in clusters are dominantly red, due to a combination of dust and quenching. Bulge galaxies in both environments are mostly red, as expected, with fewer star-forming galaxies. We caution that we cannot comment strongly on the physical processes responsible for blue and red colours within the same morphological types in different environments. Galaxy colour is strongly correlated with mass, such galaxies tend to be more red with increasing stellar mass (Kajisawa & Yamada 2006; Fang et al. 2018). As our field sample has a higher fraction of low mass galaxies than our cluster sample, this trend is likely influenced by the underlying stellar mass distribution of the galaxies.

We note that a fair number of intermediate cluster galaxies also lie near the quiescent wedge at $z \sim 1.6$. Although we use different classification methods, this is similar to the results of Kartaltepe et al. (2015), who find that while galaxies classified as mostly-spheroid and mostly-disk are well-separated into the quiescent and star-forming regions of the UVJ diagram, galaxies classified as a mix of disk and spheroid show more scatter between these regions. Our results also agree with previous work that has found galaxies in high density environments are more red and dusty (Bamford et al. 2009). Specifically, Bassett et al. (2013) also find evidence for an increased fraction of red and dusty galaxies at $z \sim 1.6$.

Chapter 5

Discussion

5.1 Qualitative morphologies and their quantitative analogs

One of the goals of this thesis was to show that quantitative measurements can be used to recover trends that have predominantly been studied using qualitative visual morphologies. In this regard, the top question one might ask when assessing our methods is: can quantitative methods reliably reproduce Hubble sequence morphologies? Our answer is, technically, no. In the following section, we will explore how both qualitative classification and quantitative measurements of galaxy morphology are indefinite and highly dependent on observations. However, we will also explore why visual classifications themselves are not truly reliable, and how quantitative measurements offer many strengths of their own. Hopefully, we will show why our position remains that quantitative methods are a powerful tool in the study of galaxy properties and evolution.

Before we continue a discussion of qualitative and quantitative methods, we must make a clarification. We have thus far treated galaxy morphology and structure as interchangeable concepts. To be specific, quantitative measurements like Sérsic index trace galaxy structure, not morphology (van der Wel et al. 2014). Structure refers to the distribution of light and stellar mass within a galaxy. Morphology, in retrospect, is a rather ambiguously defined concept. Studies have found that visual morphology can be constrained by a galaxy's SED (Uzeirbegovic et al. 2022), and that Hubble types are better recovered by a mix of quantitative measurements and galaxy colour (Nantais et al. 2013). Galaxy colour is intrinsically

tied to SFR, star formation history, and gas content—as is the galaxy SED—which suggests that visual morphology traces not only structure, but also star formation (Tasca et al. 2009). Although structure and morphology are well-correlated in the local universe, quantitative measurements of structure only recover a fraction of the information typically used to classify visual Hubble types.

5.1.1 Morphological classifications and structural measurements are indefinite

One of the great difficulties with measuring galaxy structure is that it is not a singular, fixed, or well-defined measurement. Quantitative structural measurements of galaxies are dependent on the rest-frame wavelengths from which they are measured (Andrae et al. 2011; Vulcani et al. 2014; Cerulo et al. 2017; Bluck et al. 2019; Ferreira et al. 2023). Bluer wavelengths are biased towards younger stellar populations, highlighting areas of new star formation (Rawat et al. 2009; Conselice 2014; Huertas-Company et al. 2014). Sérsic indices, especially those of disk galaxies, are often found to be lower when measured in bluer wavelengths (Rawat et al. 2009; Buitrago et al. 2013; Vulcani et al. 2014; Gillman et al. 2020). Structural measurements can also be impacted by dust, resulting in Sérsic profiles with lower n and larger R_e (Vulcani et al. 2014). While structural parameters are most notably affected by wavelength differences, Ferreira et al. (2023) note that classifications of visual morphology can also be impacted by the wavelength of available observations.

As we seek to study high-redshift galaxies, we face more frequent observational challenges to both qualitative or quantitative methods. Morishita et al. (2014) note that it becomes more difficult to successfully fit multi-component light profiles as both galaxy size and image resolution decrease—a frequent issue in high-z studies. Surface brightness profiles appear smoother with lower image resolution, artificially hiding more complex features (Buitrago et al. 2013). These are challenges at low-z as well, as Bamford et al. (2009) coined the term "classification bias" to describe how degrading image quality resulted in Galaxy Zoo volunteers preferentially classifying galaxies as elliptical based on visual appearance. More recently, Ferreira et al. (2023) find that the improved resolution of images from the *James Webb Space Telescope* (*JWST*) can result in different visual classification of high-z

galaxies previously observed with *HST*, returning a greater fraction of galaxies with disk morphologies. At high-z, morphology and structure will also be impacted by cosmological surface brightness dimming, which scales as $(1 + z)^4$ and can wash out fainter features.

Aside from observational challenges impacting accuracy and stability, we must also consider how galaxy evolution itself can impact morphology and structure. There is mounting evidence that high-z galaxies are structurally different, such that the typical quantitative methods of CAS, Gini$-M_{20}$, and Sérsic index all perform worse at separating Hubble types of high-z galaxies (Mortlock et al. 2013; Ferreira et al. 2023). Independently, there is also evidence that the average Sérsic index of galaxies evolves over time, becoming lower at high-z (Buitrago et al. 2013; Morishita et al. 2014; Ferreira et al. 2023). However, the fault for this discrepancy may not lie entirely with the quantitative measurements. As Mortlock et al. (2013) point out, the Hubble sequence is based upon the morphologies of galaxies in the local universe, and it may not be appropriate to ascribe the same set of classifications to young, evolving galaxies in the early universe. Huertas-Company et al. (2014) find that machine learning techniques trained on low-z galaxies perform worse at classifying high-z galaxies, compared to the same technique trained on high-z galaxies. There are conflicting conclusions about the reliability of the Hubble sequence at high-z. Previous studies often claim that Hubble types are not the dominant galaxy morphologies at $z > 2$ (Mortlock et al. 2013; Conselice 2014). However, Ferreira et al. (2023) suggest that this conclusion is biased by inadequate image resolution and filter coverage, resulting in an overestimate in the number of peculiar galaxies. More high-z studies of structure and morphology are needed to resolve this.

Finally, we turn our attention to the most common method used to assess the supposed accuracy of structural measurements: comparing the relative completeness and contamination of quantitative classifications against a visually-classified sample. For example, Mei et al. (2012) compare B-band visual classifications to the Sérsic index of galaxies at $z \sim 1.3$, finding that 70 percent of early-type galaxies have $n > 2.5$ while 78 percent of late-type galaxies have $n < 2.5$. Between $0 < z < 3$, van der Wel et al. (2014) find roughly 80 percent of UVJ-selected early-type galaxies have $n > 2.5$, and likewise 80 percent of late-type galaxies have $n < 2.5$. Meanwhile, Smethurst et al. (2022) discuss the purity and

completeness of various proxy methods for morphological classification, including colour-cuts, colour-magnitude diagrams, UVJ active/passive selection, and Sérsic fits, concluding that no method simultaneously captures high completeness with low contamination when separating early- and late-type galaxies.

In most cases, however, visual classifications come with a similar amount of uncertainty. Postman et al. (2005) find agreement in $70 - 80$ percent of their visual E/S0/Sp classifications when compared to two other independent studies. Cerulo et al. (2017) find agreement between three researchers of 70 percent when considering only early- and late-type classifications, but as low as 40 percent when considering more detailed classifications. Mei et al. (2023) use visual morphologies classified by only one researcher, and simply assume an uncertainty of 70 percent as per previous studies. Modern visual classification schemes often simply require an agreement between majority of researchers ($\geq$ 50 percent) to define a galaxy's morphology (e.g. Kartaltepe et al. 2015; Ferreira et al. 2023). Quantitative methods, when applied properly, recover similar agreement in classification as many visual assessments often have with each other. This calls into question why the accuracy of quantitative methods is still regularly judged against visual classifications.

5.1.2 The strengths of quantitative measurements

Quantitative methods offer many benefits over visual classification. Goto et al. (2003) comment upon favouring quantitative methods for both their efficiency and because the use of visual classifications introduces unknown biases into the results. Indeed, the fact that quantitative methods can be automated makes them far more efficient for use with large samples. Meanwhile, errors in quantitative methods can also often be measured more directly, particularly in techniques which utilize models and residual images. In general, quantitative measurements recover more specific information than broad categorizations are capable of, and in the case of galaxy structure quantitative methods implicitly allow for a wide range of unique galaxy shapes (see Sazonova et al. 2020 as an example).

Rather than basing the accuracy of a quantitative method on how well it reproduces the Hubble sequence, we propose that the accuracy of a quantitative method should be judged on how well it separates distinct galaxy populations. Sérsic profiles are among the simplest

techniques, and generally more reliable than other quantitative methods in cases of low resolution and S/N (see Andrae et al. 2011 for a thorough comparison of quantitative techniques). While there are arguments that multi-component light profiles are more realistic, even studies with decent image resolution have found that some galaxies fail to be fit with multiple components, or are better fit by a single Sérsic profile (Ascaso et al. 2009; Nantais et al. 2013; Bluck et al. 2019). There is also a wealth of evidence that single-component Sérsic fits are capable of separating galaxy populations in n at a range of redshifts. Even accounting for the evolution of n, studies have found good correlation with Sérsic index and early-/late-type morphologies (Buitrago et al. 2013) as well as quiescence (Bell et al. 2012; Strazzullo et al. 2023) around $z \sim 1.6$.

We cannot be confident that our measurements of Sérsic index perfectly reproduce Hubble morphologies, hence why we avoid labelling our classifications using elliptical/spiral or early-/late-type. However, this does not mean that our quantitative methods are inaccurate. Our results indicate that our cuts in n have successfully recovered distinct galaxy populations, which differ in their relationships with environment, stellar mass, and colour. We have shown that even simple quantitative methods can effectively recover trends in the morphology-density relation at high-z, and we encourage further use of quantitative methods in the study of galaxy evolution at high redshift.

5.2 Comparisons with previous morphology-density studies

In Chapter 1, we summarized three papers that we consider to be flagship studies of the morphology-density relation up to $z \sim 1$. Studies of the relationship between galaxy morphology, structure, and density extend far beyond the work of Dressler (1980), Dressler et al. (1997), and Postman et al. (2005), including various samples, redshifts, and methodologies. Unfortunately, the range of methods employed by different studies, including variations in both morphological classifications and density measurements, makes direct comparison difficult in many cases. In this section, we will summarize some of the key findings of these studies across cosmic time, with particular attention to how our own results fit into this

broader context.

Evolution in the morphology-density relation was first noted by a change in the fraction of lenticular galaxies around $z \sim 0.5$ (Dressler et al. 1997; Fasano et al. 2000; Goto et al. 2003), and confirmed up to $z \lesssim 1$ (Postman et al. 2005; Cerulo et al. 2017; Cavanagh et al. 2023). As the fraction of lenticular galaxies decreases with redshift, studies have noted a proportional increase in the fraction of spiral galaxies at high-z. Poggianti et al. (2008) also find that the fraction of lenticular galaxies at $z \sim 0.5$ is less dependent on galaxy density, such that it remains roughly flat at 20 percent. In comparison, we do find a higher overall fraction of disk-like galaxies at $z \sim 1.6$ than visual spiral galaxies found at low-z—however, we cannot comment significantly on this difference as it is undoubtedly influenced by differences in morphological classification. Of the studies mentioned above, only Goto et al. (2003) and Cerulo et al. (2017) use quantitative classification methods, both of which differ from our own. We conclude only that there may be evidence for a higher fraction of spirals/late-types at $z \sim 1.6$, and we leave further discussion of lenticular galaxies to Section 5.4.

A number of studies have found evidence that the morphology-density relation may behave differently in regions of intermediate density, such as loose clusters or groups. Fasano et al. (2000) suggest that the difference in the relation between low- and high-concentration clusters in the local universe may indicate that different physical processes dominate in different environments. Goto et al. (2003) are the first to directly incorporate field galaxies into the morphology-density relation, by placing no environmental requirements on their sample, and find evidence up to $z \sim 0.5$ that trends in galaxy morphology differ between intermediate-density and high-density regions. In a $z = 0.84$ cluster, Nantais et al. (2013) find that the greatest change in morphological fractions occurs between low- and intermediate-density regions, before galaxies begin to approach the dense cluster center. While we do not directly study intermediate-density regions (such as galaxy groups or cluster outskirts), the differences we find between cluster and field environments at $z \sim 1.6$ lends support to the notion the morphology-density relation may behave differently in different types of environments, potentially due to differences in dominant environmental processes.

Multiple studies have suggested that a relationship between morphology and stellar mass may influence trends in the morphology-density relation. In the local universe, Bamford

et al. (2009) suggest that as much as 30 − 40 percent of the observed morphology-density relation may be driven primarily by differences in stellar mass. At $0.4 < z < 0.6$, Huertas-Company et al. (2009) find that the speed of morphological transformation in cluster galaxies may be dependent on their stellar mass. Tasca et al. (2009) further suggest that environmental influences on morphology may be stronger at lower stellar masses. Cerulo et al. (2017) also find a dependence on stellar mass for morphological fractions in clusters in both the local universe and $0.8 < z < 1.5$. In contrast, Holden et al. (2007) find that for $z < 0.83$, the fraction of early-type galaxies is independent of mass above $M_* > 10^{10.6} M_\odot$, but that below $M_* < 10^{10.6} M_\odot$ their luminosity-selected sample is dominated by late-type galaxies. Our results at $z \sim 1.6$ further support the idea that the effects of environment on morphology are intertwined with the effects of stellar mass, but confirm that stellar mass is not solely responsible for the morphology-density relation.

We would be remiss to conclude this section without highlighting the work of Tasca et al. (2009), who perform a comprehensive study on the evolution of the morphology-density relation from $z = 0.2$ to $z = 1$ using quantitative measurements of morphology. Their study is one of the few that can make direct comments on the evolution of the relation through cosmic time, as they take steps to apply the same methodology to their entire sample, including calculating densities such that they are invariant to redshift, and separating their sample into bins of stellar mass and magnitude. With their results, Tasca et al. (2009) confirm what other studies have suggested: that the morphology-density relation is flatter at $z \sim 1$ than at lower redshifts. Our own study unfortunately suffers from the same limitation as many others, in that we cannot make direct comparison due to differing methods in both morphological classification and local density. Qualitatively, the change in our cluster disk-like fraction from low to high density suggests that our relation may also be flatter at $z \sim 1.6$ than low-z, although we stress that we cannot definitively conclude this in the same way that Tasca et al. (2009) do for $z \sim 1$.

5.2.1 Galaxy morphology in clusters at $z \sim 1.6$

For many years, studies of the morphology-density relation above $z > 1$ have been limited by our ability to detect high-z clusters and obtain images with enough resolution to reliably classify morphology. In this section, we compare our results to the handful of studies on morphology and environment which cover a similar redshift range to $z \sim 1.6$ to determine whether we find consistent results. We summarize the methods of these studies before briefly comparing results with our own.

Sazonova et al. (2020) study the structural properties of galaxies in four clusters from $1.2 < z < 1.8$ using a variety of quantitative measurements in the rest-frame V-band. Their results are mixed, although they note this could be due to two of the clusters in their sample which may be a complex, non-standard system consisting of a cluster and a protocluster or group connected by filaments. If we consider instead only their two standard clusters at $z = 1.19$ and $z = 1.75$, they find that cluster galaxies have higher Sérsic indices, concentration, and bulge strength compared to field galaxies.

Bassett et al. (2013) study a forming $z \sim 1.6$ cluster found within the CANDELS UDS field. They use Sérsic fits in F125W (rest-frame B-band), defining galaxies with $n > 2$ as bulge-dominated and $n < 2$ as disk-dominated. They primarily analyze the relationship between both galaxy morphology and quenched fraction on the projected radius from the center of the cluster, but also comment on the effects of stellar mass. In general, they find that star-forming galaxies look similar in both cluster and field galaxies, but that quiescent galaxies in the cluster have larger effective radii and smaller n than those in the field. While they find no significant trends in the morphology-radius relation in this cluster, they do find an enhanced fraction of quenched galaxies in the cluster compared to the field.

Strazzullo et al. (2023) study five massive clusters at $1.4 < z < 1.7$, using Sérsic fits in F140W for cluster galaxies and comparing to F160W fits from van der Wel et al. (2012) for field galaxies. We share the most similar morphological classifications with Strazzullo et al. (2023), who also categorize galaxies with $n > 2.5$ as bulge-dominated, $n < 1.5$ as disk-dominated, and $1.5 < n < 2.5$ as intermediate. When comparing cluster to field, they correct for measured R_e between F140W and F160W, but note that corrections to n fall within uncertainties and do not impact results. Most galaxies in their sample lack photometric

redshifts as their clusters have photometry only in four bands. Instead, they select cluster members via colours and use background subtraction to correct morphological fractions. We also note that their field comparison includes CANDELS UDS, however, Strazzullo et al. (2023) do not comment on the cluster at $z \sim 1.6$ within the UDS field (studied by Bassett et al. 2013).

The final study we compare to is Mei et al. (2023), who study 16 clusters from $1.3 < z < 2.8$ using visual morphologies, and compare to field galaxies from GOODS-S with morphologies classified by Kartaltepe et al. (2015). They have one researcher classify morphology in F140W for all clusters, which ranges from rest-frame V-band at $z = 1.3$ to rest-frame U-band at $z = 2.8$. Visual field morphologies are primarily classified in F160W. Mei et al. (2023) calculate local density using 7th-Nearest Neighbours, however, their clusters only have photometric coverage in three to five bands, so they also lack photometric redshifts. To account for this, they instead restrict analysis to the cluster cores, using colour-cuts to remove most $z < 1.3$ galaxies and background subtraction to correct morphological fractions. They study the relations of both morphology and quenched fraction with local density, and attempt to analyze the relation with stellar mass.

Our morphology-density results qualitatively agree with those of Mei et al. (2023), who find that the morphology-density relation is in place at $z \sim 1.6$. The differences between visual classification and Sérsic index methodology do not seem to strongly impact the observed trend, possibly since Mei et al. (2023) consider only early-type and late-type classifications. Sazonova et al. (2020) and Strazzullo et al. (2023) do not directly measure local galaxy density nor clustercentric radius, but we note that they also find evidence of a high-z morphology-density relation in their results. For example, Sazonova et al. (2020) find that the inner 50 percent of members in their $z = 1.75$ cluster have higher n than the outer 50 percent.

In terms of stellar mass, our work agrees with the results of Strazzullo et al. (2023), who find that high mass galaxies at $z \sim 1.5$ are predominantly bulge-dominated ($n > 2.5$). In contrast, Mei et al. (2023) find a weak dependence on morphology and quenched fraction with galaxy stellar mass, however, they caution that their stellar mass estimates have large uncertainties due to lack of IR coverage in their clusters. We also point out that significant trends with stellar mass may be difficult to detect in Mei et al. (2023) as they bin their data

into only two broad stellar mass bins. While Bassett et al. (2013) do not comment directly on differences with environment, they do find that $n > 2.5$ galaxies are more likely to be high-mass and quenched. Ours is the only study to directly show that the morphology-mass relation is different in the cluster environment than the field at high-z.

We differ from Mei et al. (2023), Strazzullo et al. (2023), and Bassett et al. (2013) in that we do not comment on the quiescent galaxy fraction as a function of environment.Nantais et al. (2017) find that the quenched fraction in CDFS44, XMM105, and XMM113 is only marginally higher than the field at $z \sim 1.6$ (42 percent of galaxies are quenched in the clusters versus 32 percent in the field), which is significantly lower than the observed quenched fractions at lower redshifts. At face value, the quenched fraction in our clusters also appears to be lower than that found in $z \sim 1.6$ clusters of similar studies—although we note that this comparison may be impacted by differences in stellar mass limits, as well as choice of filters and colour cuts used in UVJ alternatives (such as Mei et al. 2023 and Strazzullo et al. 2023). Nantais et al. (2017) also suggest that quenched fractions may be influenced by both total halo mass and halo age. We do not have measurements for the halo mass of our three clusters from which we could compare with the results of Mei et al. (2023), so we cannot comment further on this. We refer the reader to Nantais et al. (2017) for further discussion on the quenched galaxy fraction in our clusters.

We note that one of our biggest strengths over the studies mentioned here is our access to spectroscopic and photometric galaxy redshifts, which has allowed us both robust determination of cluster and field members, as well as accurate local density measurements without the need for colour cuts or background subtraction. Additionally, with the wealth of photometric data on our clusters, we have higher accuracy in our stellar mass estimates, which has allowed us to detect significant trends in the morphology-mass relation in cluster and field environments. Although we do not cover as wide a range in redshift as Mei et al. (2023), our three clusters have very similar redshifts, such that we are confident our morphological measurements are not biased due to differences in rest-frame wavelengths within our own sample. Despite differences in methodology, we conclude overall that our main results are consistent with previous work at $z \sim 1.6$.

5.3 Physical origins of the morphology-density relation

In this section, we discuss common physical processes thought to drive the morphology-density relation and assess their likely influence at $z \sim 1.6$ in light of our results. We will begin by discussing processes which may drive the fraction of bulge galaxies up and the fraction of disk galaxies down in cluster environments. We will then explore which processes may explain the difference in the morphology-mass relation between cluster and field galaxies.

5.3.1 The transformation of disks and bulges in clusters

Ram pressure stripping is often one of the most popular theories when discussing cluster-specific environmental processes (Gunn & Gott 1972). Clusters are filled with hot X-ray gas called the intracluster medium (ICM). As galaxies move through the cluster, the ICM acts as a "wind" which strips loosely-bound material from the galaxy such as gas and dust. The strength of ram pressure stripping is proportional to both the square of the galaxy's velocity as well as the density of gas in the ICM, which is expected to be lower in young cluster environments. While ram pressure stripping can cause rapid outside-in quenching, it does not directly induce a change in morphology (D'Onofrio et al. 2015; Sazonova et al. 2020). It is therefore unlikely that ram pressure stripping is the dominant mechanism behind morphological transformation in our $z \sim 1.6$ clusters.

Strangulation is a process that results in slower quenching of star formation in galaxies entering the cluster environment (Larson et al. 1980; Balogh et al. 2000). As a galaxy falls into the gravitational potential of the cluster, it loses hold on the reservoir of gas in its halo. Unlike what may happen during ram pressure stripping, the galaxy continues to hold on to some gas in its disk and core, and maintains star formation until it slowly uses up its gas. As this quenching process occurs on a much longer timescale, strangulation could influence slow morphological changes in star-forming galaxies entering cluster environments for the first time—although it is difficult to quantify what overall impact strangulation may have on morphology.

Galaxy harassment describes the effects of repeated, high-speed fly-by interactions of galaxies (Moore et al. 1996). These types of interactions are more frequent in clusters than

other environments, since galaxy densities and relative speeds are both high. Harassment can cause not only tidal stripping of mass from the outskirts of galaxies, but can also have a direct influence on morphology, resulting in disturbed appearances with higher asymmetry and increased presence of features such as warps, bars, and tidal tails. While harassment depends on both galaxy density and stellar mass, Bialas et al. (2015) find that the timescales required to fully transform galaxies via harassment (> 5 Gyr) are too long to be effective for galaxies which have only recently been accreted into the cluster. D'Onofrio et al. (2015) suggest that galaxy harassment may strip the extended stellar envelopes of ellipticals in cluster cores, resulting in lower observed n and R_e than ellipticals on the outskirts of clusters.

Major mergers are considered to be one of the primary mechanisms responsible for the formation of elliptical galaxies (Mihos & Hernquist 1994). A merger between two spiral galaxies of similar mass can disrupt the ordered rotation of stars in their disks, leading to the random velocities associated with elliptical galaxies. Wet mergers (involving gas-rich galaxies) can induce intense bursts of new star formation, while dry mergers (involving gas-poor galaxies) primarily redistribute pre-existing stellar mass from the original galaxies into a single post-merger galaxy. Lin et al. (2010) find that dry mergers are preferentially found in high-density environments due to the relative abundance of quenched and early-type galaxies. Goto et al. (2003) suggest that mergers may be responsible for driving the fraction of elliptical galaxies in high-density environments at low- and intermediate-z. However, mergers are in fact expected to be less common in cluster environments due to high velocity dispersions (Just et al. 2010; Bekki & Couch 2011; Mei et al. 2012). Pfeffer et al. (2023) find low relative merger rates in high-density environments in the EAGLE simulation. Delahaye et al. (2017) also confirm that the merger rates in our $z \sim 1.6$ clusters are roughly the same or lower than that of the field, meaning that mergers within the cluster environment are unlikely to drive the morphology-density relation in our clusters.

In contrast, galaxy group environments host above-average galaxy densities and have lower velocity dispersions than clusters, both of which encourage mergers. Group pre-processing has been proposed as a process by which galaxies are first morphologically transformed in a group environment, which then falls into the cluster at later times (Wetzel et al. 2013). Sazonova et al. (2020) find that group pre-processing is a possible dominant

mechanism driving the morphology-density relation at $z \sim 1.5$. Delahaye et al. (2017) suggest a similar mechanism to explain the morphologies of cluster galaxies with low merger rates, but alternatively propose that protocluster may be a favourable environment for preprocessing spirals into ellipticals. Like nearby galaxy groups, high-z protoclusters are expected to be more dense than the field, but with lower relative velocities than their future virialized counterparts. If elliptical galaxies in clusters are the result of early transformations in the protocluster stage, that may explain why there is little evolution in the elliptical galaxy fraction with redshift for $z < 2$.

One of the more recently suggested processes for environmental quenching is overconsumption (McGee et al. 2014). Overconsumption proposes that when a galaxy is cut off from inflows of new gas, such as during infall into a cluster, its quenching timescale will depend not only on the quantity of gas left within the galaxy (as in strangulation), but also on its SFR and mass-loading factor. The mass-loading factor describes the rate of additional gas outflow caused by star formation, and has itself been found to be a function of mass (McGee et al. 2014). When SFR is high, overconsumption is likely to quench galaxies faster than most external, dynamical stripping mechanisms. Kawinwanichakij et al. (2017) also propose that overconsumption can explain why environmental quenching is more efficient for galaxies with higher stellar mass at $z > 1$. The combination of environmental factors (required to cut off gas inflows) and mass-dependence may make overconsumption a favourable process to explain our observed morphology-mass relation at $z \sim 1.6$.

5.3.2 Morphology and stellar mass

It is well-known that galaxy stellar mass increases with local density (Kauffmann et al. 2004; Bamford et al. 2009; Huertas-Company et al. 2009; Muzzin et al. 2012; Mortlock et al. 2015; Pfeffer et al. 2023). Both van der Wel (2008) and D'Onofrio et al. (2015) find that Sérsic index is strongly linked to stellar mass, while Bluck et al. (2019) find that galaxy stellar mass is a better predictor of *B/T* ratio than local environment (although we note that they measure *B/T* from stellar mass rather than light distribution). This makes it imperative when studying the morphology-density relation to ask whether the relation is driven primarily by environment or by stellar mass.

In Section 4.3, we indeed find a strong relationship between morphology and galaxy stellar mass in clusters. However, we also find (as in Figures 4.5 and 4.6) that the morphology-mass relationship is not universal across all environments at $z \sim 1.6$. We are not the only study to find that morphology depends on both stellar mass and environment. Tasca et al. (2009) find that the morphology-density relation holds in cluster galaxies with $M_* < 10^{10.6} M_\odot$, but that above this mass, morphology does not depend on local environment. Meanwhile, Calvi et al. (2012) find that for $M_* < 10^{11} M_\odot$, clusters are the only environment where morphology is mass-dependent, while morphology of non-cluster galaxies is dependent on both mass and global environment for $M_* > 10^{11} M_\odot$. Nantais et al. (2013) find that both high-mass galaxies in low-density environments and low-mass galaxies in high-density environments have morphological fractions in-between what is found when considering only the influence of mass or environment.

As with bulge-like morphologies, many studies have found higher rates of galaxy quenching in high density environments (Poggianti et al. 2008; Bassett et al. 2013; Kawinwanichakij et al. 2017; Taylor et al. 2023). There is also a strong relationship between Sérsic index and galaxy quiescence (Bell et al. 2012; Morishita et al. 2014; van der Wel et al. 2014; Kawinwanichakij et al. 2017; Matharu et al. 2019), such that a transition from disk-like to bulge-like morphology may be considered a strong sign of star formation quenching in a galaxy. We will utilize the much-studied relationship between quenching, mass, and environment to explore the physical mechanisms which may also drive a relationship with morphology.

Peng et al. (2010b) first suggested that "mass quenching" and "environmental quenching" could be considered distinct and separable processes up to $z \sim 1$. Muzzin et al. (2012) found that while mass quenching was indeed independent of environment in $z \sim 1$ clusters, environmental quenching was not independent of galaxy mass. Above $z > 1$, it has become clear that environmental quenching is not separable from mass quenching—that is, environmental quenching depends on stellar mass (Kawinwanichakij et al. 2017; van der Burg et al. 2020).

We have noted that $M_* \approx 10^{10.8} M_\odot$ appears to be a transitional value in the morphology-mass relationship of field galaxies, such that the fraction of disk-like galaxies decreases rapidly above this mass (as seen in Figure 4.5). This value is roughly consistent with the characteristic stellar mass of star-forming galaxies found in many studies of the stellar mass

function (SMF) (Peng et al. 2010b; van der Burg et al. 2013; McLeod et al. 2021; Taylor et al. 2023). The SMF represents the relative number density of galaxies as a function of stellar mass, while the the characteristic stellar mass can be seen as representative of a turning-point in the SMF, above which the number density of galaxies sharply declines. Nantais et al. (2016) construct the SMF at $z \sim 1.5$ with a sample including our three clusters, and find a characteristic stellar mass of $10^{10.71} M_{\odot}$ and $10^{10.94} M_{\odot}$ for star-forming galaxies in the field and cluster respectively. This suggests an intrinsic stellar mass above which galaxies may be preferentially quenched—theoretically by mass-quenching mechanisms. The fact that the turning point in our morphology-mass relation is consistent with these reported values may suggest that the same process responsible for mass-quenching could also be responsible for structural changes between disk-like and bulge-like morphologies in the field.

Feedback from an active galactic nucleus (AGN) has been suggested as a primary process for quenching high-mass galaxies (Peng et al. 2010b; Bell et al. 2012; Muldrew et al. 2018; Joshi et al. 2020). The mass of a supermassive black hole at the center of galaxies is strongly linked to the mass of the galaxy's central bulge component, and is also one of the properties that determines the maximum power of its AGN (Bower et al. 2006). AGN feedback can prevent gas from cooling in the galaxy, thus shutting off star formation, and has also been linked to galaxies losing their disk-like morphologies in simulations (Joshi et al. 2020).

In the absence of environmental processes, we consider AGN feedback to be a likely candidate for morphological transformation of high-mass galaxies in the field.

5.4 The evolution of lenticular galaxies

A notable morphological classification missing from our analysis in comparison to other flagship studies is that of lenticular galaxies. We choose not to focus our efforts on distinguishing the lenticular galaxy population for two main reasons. Firstly, lenticular galaxies are often difficult to distinguish from elliptical galaxies, especially at high redshifts (Bamford et al. 2009; Buitrago et al. 2013; Cerulo et al. 2017). While lenticular galaxies in the

local universe have typical Sérsic indices lower than average ellipticals and higher than average spirals (D'Onofrio et al. 2015; Cerulo et al. 2017), they have a wide distribution in n such that they commonly overlap with both populations (Gao et al. 2018; Deeley et al. 2020). Secondly, the fraction of lenticular galaxies has been found to decrease with redshift (Dressler et al. 1997; Fasano et al. 2000; Goto et al. 2003; Postman et al. 2005; Poggianti et al. 2009; Just et al. 2010; D'Onofrio et al. 2015; Cavanagh et al. 2023). Even if we could cleanly separate lenticular galaxies, we may not find a significant fraction of them at $z \sim 1.6$.

However, lenticular galaxies have historically played an important role in the study and understanding of the morphology-density relation as discussed in Section 5.2, and we would be remiss not to comment on their significance and physical origins. Postman et al. (2005) suggest that the difference in morphology-density relation of elliptical and lenticular galaxies at $z \sim 1$ indicates that the physical processes driving their morphologies must act on different timescales. It is interesting to note that despite Hubble's initial classification, lenticular galaxies themselves are not a homogeneous population. Both simulations and observational studies have suggested two major pathways for the transformation of spirals into lenticular galaxies, which lead to differences in the observed properties of lenticulars (Bekki & Couch 2011; Moran et al. 2007; Deeley et al. 2020, 2021; Cavanagh et al. 2023; Pfeffer et al. 2023). As our key interest is the morphology-density relation, we will use literature to explore how each pathway depends on environment.

Within the IllustrisTNG cosmological simulation, Joshi et al. (2020) find that mergers play a significant role in the morphological transformation of disk galaxies in the field, but not in clusters. The properties of lenticulars in low-density environments have been found to differ from those in high-density environments, including: larger bulges (Bekki & Couch 2011); higher n and smaller R_e (Deeley et al. 2020); older stellar populations, particularly in the core (Gao et al. 2018; Deeley et al. 2020, 2021; Cavanagh et al. 2023); as well as higher pressure support and lower rotational support (Deeley et al. 2020). If lenticular galaxies form from spirals, minor mergers would be necessary to contribute to the build up of significant bulges (Bekki & Couch 2011; Gao et al. 2018) as well as increase n (D'Onofrio et al. 2015). Mergers and tidal interactions could also explain why the rotation of gas in these galaxies is often misaligned with that of their stars (Deeley et al. 2021). Using simulations, Tapia et al. (2017) show that mergers taking place at $z = 1.8 - 1.5$ are capable of

producing lenticular galaxies that agree with the Tully-Fisher relation and observed lenticular properties by $z = 0$. Deeley et al. (2021) and Pfeffer et al. (2023) trace the history of $z \sim 0$ lenticular galaxies in IllustrisTNG and EAGLE, finding that many lenticular galaxies in low-density environments undergo mergers prior to their morphological transformation. While mergers are less common in dense clusters, Gao et al. (2018) suggest that at least some lenticular galaxies could be pre-processed in galaxy groups.

In comparison, most lenticular galaxies in clusters have thinner disks (Bekki & Couch 2011), lower n (Deeley et al. 2020), lower masses (Cavanagh et al. 2023), bluer cores (Deeley et al. 2021; Cavanagh et al. 2023), a mix of star formation (Cavanagh et al. 2023), and high rotational support (Deeley et al. 2020). Deeley et al. (2020) particularly find that lenticulars in high-density environments have light concentrations and kinematics more similar to that of spiral galaxies. Cluster infall has been suggested to transform spiral galaxies by rapidly stripping them of gas (Moran et al. 2007), and cosmological simulations have shown that this process is indeed linked to a second formation pathway for lenticular galaxies (Deeley et al. 2021; Pfeffer et al. 2023). At $z \sim 1$, Matharu et al. (2021) find evidence that galaxies entering clusters are rapidly quenched by an outside-in process. Bassett et al. (2013) find evidence of quenched galaxies with low n on the outskirts of a cluster at $z \sim 1.6$, reminiscent of rapidly-quenched spirals. Meanwhile at $1 < z < 1.4$, Chan et al. (2021) observe an increase of oblate quiescent galaxies with intermediate stellar masses in clusters compared to the field. Ram pressure stripping could efficiently explain this transformation of spirals to lenticulars in clusters, including very little change in overall structure and outside-in quenching resulting in bluer cores than disks. The strength of ram pressure stripping should increase as clusters build up ICM, which may explain why lenticular galaxies in clusters are more prevalent at lower redshifts—and why lenticular galaxies follow the morphology-density relation.

Chapter 6

Conclusions

We study the morphology-density relation, morphology-mass relation, and UVJ colours of galaxies at $z \sim 1.6$ in three SpARCS clusters (CDFS44, XMM105, and XMM113) and two 3D-HST/CANDELS fields (COSMOS and GOODS-S). We fit the F160W light profiles of galaxies to single-component Sérsic profiles and use the Sérsic index, n, as a quantitative measurement of morphology. We define disk-like galaxies as those with $n < 1.5$, intermediate galaxies as $1.5 < n < 2.5$, and bulge-like galaxies as $n > 2.5$. We calculate projected local densities using 5th-Nearest Neighbours with $\Delta v = 3000$ km/s, using a mix of spectroscopic, grism, and photometric redshifts.

Through direct comparison of cluster and field environments, we find the following at $z \sim 1.6$:

1. Single-component Sérsic fits are a quantitative measurement that can effectively reveal trends in galaxy structure similar to those found in studies using visual Hubble morphologies.

2. A relationship between morphology and local galaxy density exists within clusters, such that the fraction of disk-like galaxies decreases and the fraction of bulge-like galaxies increases with increasing density.

3. We find no conclusive evidence of a morphology-density relation across the majority of galaxies in the field environment. Field galaxies residing in moderate local densities ($\Sigma_5 \approx 30$ gal/Mpc^2) have a similar morphological distribution as low-density

cluster galaxies.

4. Galaxy morphologies in clusters show a strong relationship with galaxy stellar mass. The fraction of disk-like cluster galaxies decreases smoothly with increasing stellar mass, while the fraction of bulge-like cluster galaxies increases proportionally. Environmental processes driving morphological changes are mass-dependent.

5. The morphology of field galaxies with $\log(M_*/M_\odot) < 10.8$ is only weakly correlated with stellar mass, such that the fraction of disk-like galaxies decreases from approximately 60 to 50 percent and the fraction of bulge-like galaxies increases from approximately 20 to 35 percent. Above $\log(M_*/M_\odot) > 10.8$, the fraction of disk-like galaxies in the field declines sharply with stellar mass. This may be driven primarily by AGN feedback.

6. Clusters have a higher proportion of red and dusty galaxies than the field in all morphological groups. This is likely a combination of environmental processes and stellar mass differences.

7. Intermediate galaxy morphologies ($1.5 < n < 2.5$) show the weakest dependence of all morphological types on both local galaxy density and stellar mass, remaining around 15 to 25 percent for both.

Appendix A

Cluster uniqueness

For those curious, we include here a set of additional scatter plots showing the distribution of individual galaxies from each cluster and field in Sérsic index, local density, and stellar mass. Figure A.1 shows the distribution of n vs. local galaxy density, while Figure A.2 shows the distribution of n vs. galaxy stellar mass. These plots are used to explore whether any individual cluster or field has a unique distribution of galaxies which may bias our overall results from Chapters 4.2 and 4.3.

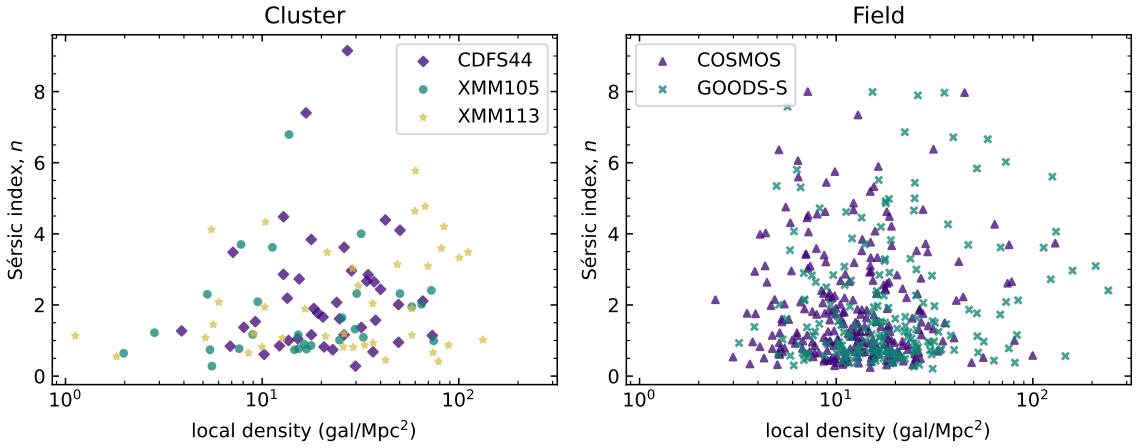

Figure A.1: The distribution of Sérsic index, n, vs local density, Σ_5, for each galaxy in the cluster and field samples. On the left, purple diamonds are cluster galaxies from CDFS44, green circles are from XMM105, and yellow stars are from XMM113. On the right, purple triangles are field galaxies from COSMOS, while green X's are from GOODS-S.

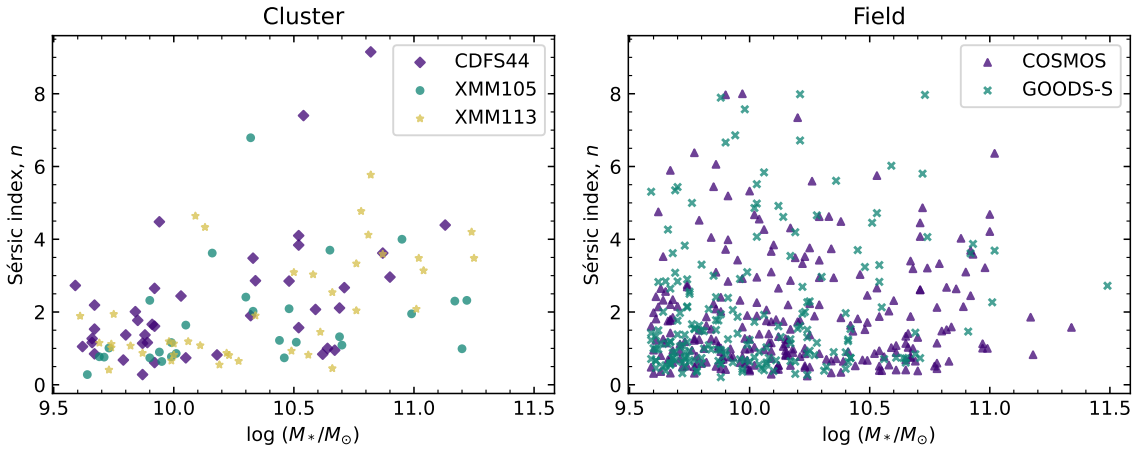

Figure A.2: The distribution of Sérsic index, n, vs stellar mass, $\log(M_*/M_\odot)$, for each galaxy in the cluster and field samples. Markers are the same as Figure A.1.

We note from Figure A.1 that the majority of the highest-density cluster galaxies are located in XMM113, while the majority of highest-density field galaxies are located within the GOODS-S field. We also note how the number of field galaxies drops noticeably above $\Sigma_5 \gtrsim 40$ gal/Mpc^2.

Appendix B

Piecewise-linear fits to the morphology-mass relation

In Figure B.1, we include a simple example of a piecewise-linear fit to the morphology-stellar mass relation. We have used linear regression to fit two sets of lines to both cluster and field samples: the lines in the upper panels are fit only to the data with $\log(M_*/M_\odot) \leq 10.8$, while the lines in the lower panels are fit to the data with $\log(M_*/M_\odot) > 10.8$.

We present the parameters for each of these linear fits in Table B.1. It is more clear with this piecewise method that both cluster and field trends undergo a change in slope about $\log(M_*/M_\odot) \approx 10.8$, although the change is more drastic in the field environment than in clusters. In both environments, the fraction of disk-like galaxies declines more steeply above $\log(M_*/M_\odot) > 10.8$.

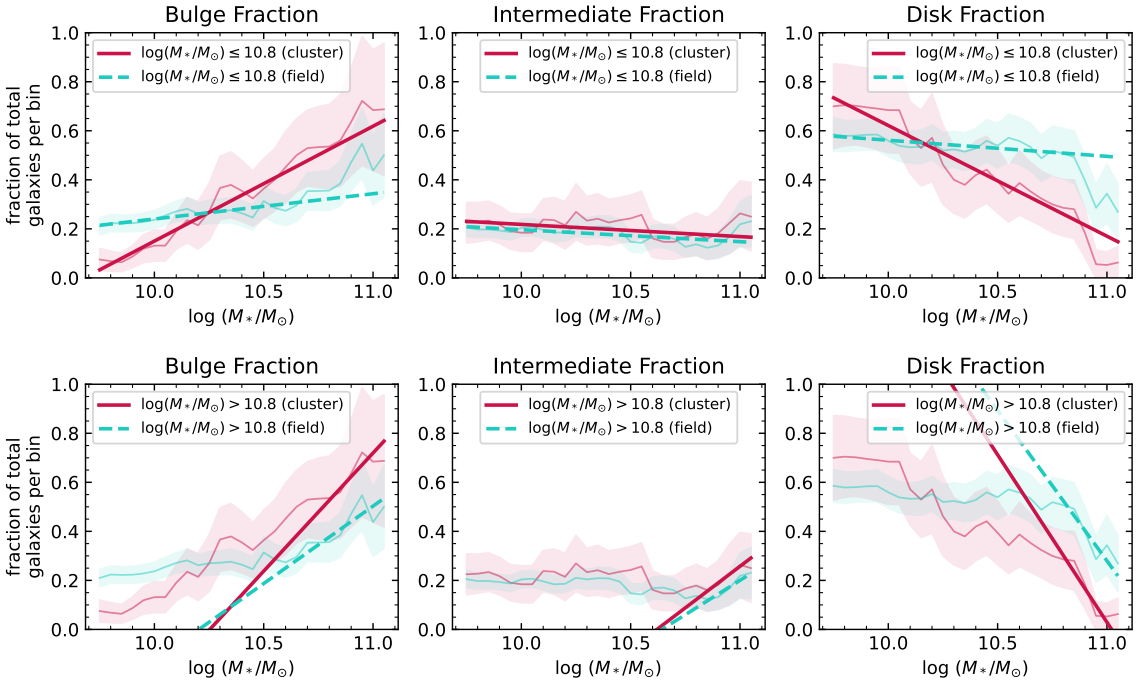

Figure B.1: Lines of best fit to each morphology-stellar mass trend for the cluster (solid red) and field samples (dashed cyan). In the upper panels, linear regression is used only on the points with $\log(M_*/M_\odot) \leq 10.8$. In the bottom panels, linear regression is used only on the points with $\log(M_*/M_\odot) > 10.8$.

	Cluster		**Field**	
Fraction	**Slope**	**Intercept**	**Slope**	**Intercept**
$\log(M_*/M_\odot) \leq 10.8$				
Bulge	0.47 ± 0.03	-4.5 ± 0.3	0.10 ± 0.01	-0.8 ± 0.1
Intermediate	-0.05 ± 0.02	0.7 ± 0.2	-0.05 ± 0.01	0.7 ± 0.1
Disk	-0.45 ± 0.03	5.1 ± 0.3	-0.07 ± 0.02	1.2 ± 0.2
$\log(M_*/M_\odot) > 10.8$				
Bulge	1.0 ± 0.4	-10 ± 4	0.6 ± 0.6	-6 ± 6
Intermediate	0.68 ± 0.07	-7.2 ± 0.8	0.6 ± 0.1	-6 ± 2
Disk	-1.4 ± 0.5	15 ± 6	-1.2 ± 0.6	14 ± 6

Table B.1: Linear regression parameters of the piecewise-linear fits from Figure B.1. Morphological fractions are given as a function of $\log(M_*/M_\odot)$.

Bibliography

Abraham, R. G., van den Bergh, S., & Nair, P. 2003, Astrophys. J., 588, 218

Andrae, R., Jahnke, K., & Melchior, P. 2011, Mon. Not. R. Astron. Soc., 411, 385

Ascaso, B., Aguerri, J. A. L., Moles, M., Sánchez-Janssen, R., & Bettoni, D. 2009, Astron. Astrophys., 506, 1071

Baldry, I. K., Balogh, M. L., Bower, R. G., Glazebrook, K., Nichol, R. C., Bamford, S. P., & Budavari, T. 2006, Mon. Not. R. Astron. Soc., 373, 469

Balogh, M. L., Navarro, J. F., & Morris, S. L. 2000, Astrophys. J., 540, 113

Bamford, S. P., Nichol, R. C., Baldry, I. K., Land, K., Lintott, C. J., Schawinski, K., Slosar, A., Szalay, A. S., Thomas, D., Torki, M., Andreescu, D., Edmondson, E. M., Miller, C. J., Murray, P., Raddick, M. J., & Vandenberg, J. 2009, Mon. Not. R. Astron. Soc., 393, 1324

Barden, M., Häußler, B., Peng, C. Y., McIntosh, D. H., & Guo, Y. 2012, Mon. Not. R. Astron. Soc., 422, 449

Bassett, R., Papovich, C., Lotz, J. M., Bell, E. F., Finkelstein, S. L., Newman, J. A., Tran, K.-V., Almaini, O., Lani, C., Cooper, M., Croton, D., Dekel, A., Ferguson, H. C., Kocevski, D. D., Koekemoer, A. M., Koo, D. C., McGrath, E. J., McIntosh, D. H., & Wechsler, R. 2013, Astrophys. J., 770, 58

Bekki, K. & Couch, W. J. 2011, Mon. Not. R. Astron. Soc., 415, 1783

Bell, E. F., van der Wel, A., Papovich, C., Kocevski, D., Lotz, J., McIntosh, D. H., Kartaltepe, J., Faber, S. M., Ferguson, H., Koekemoer, A., Grogin, N., Wuyts, S., Cheung, E., Conselice, C. J., Dekel, A., Dunlop, J. S., Giavalisco, M., Herrington, J., Koo, D. C., McGrath, E. J., de Mello, D., Rix, H.-W., Robaina, A. R., & Williams, C. C. 2012, Astrophys. J., 753, 167

Bertin, E. & Arnouts, S. 1996, Astron. Astrophys. Suppl. Ser., 117, 393

Bialas, D., Lisker, T., Olczak, C., Spurzem, R., & Kotulla, R. 2015, Astron. Astrophys., 576, A103

Bluck, A. F. L., Bottrell, C., Teimoorinia, H., Henriques, B. M. B., Mendel, J. T., Ellison, S. L., Thanjavur, K., Simard, L., Patton, D. R., Conselice, C. J., Moreno, J., & Woo, J. 2019, Mon. Not. R. Astron. Soc., 485, 666

Bower, R. G., Benson, A. J., Malbon, R., Helly, J. C., Frenk, C. S., Baugh, C. M., Cole, S., & Lacey, C. G. 2006, Mon. Not. R. Astron. Soc., 370, 645

Brammer, G. 2019, Grizli: Grism redshift and line analysis software, Astrophysics Source Code Library, record ascl:1905.001

Brammer, G. B., van Dokkum, P. G., & Coppi, P. 2008, Astrophys. J., 686, 1503

Brammer, G. B., van Dokkum, P. G., Franx, M., Fumagalli, M., Patel, S., Rix, H.-W., Skelton, R. E., Kriek, M., Nelson, E., Schmidt, K. B., Bezanson, R., da Cunha, E., Erb, D. K., Fan, X., Förster Schreiber, N., Illingworth, G. D., Labbé, I., Leja, J., Lundgren, B., Magee, D., Marchesini, D., McCarthy, P., Momcheva, I., Muzzin, A., Quadri, R., Steidel, C. C., Tal, T., Wake, D., Whitaker, K. E., & Williams, A. 2012, Astrophys. J. Suppl. Ser., 200, 13

Brinchmann, J., Charlot, S., White, S. D. M., Tremonti, C., Kauffmann, G., Heckman, T., & Brinkmann, J. 2004, Mon. Not. R. Astron. Soc., 351, 1151

Buitrago, F., Trujillo, I., Conselice, C. J., & Häußler, B. 2013, Mon. Not. R. Astron. Soc., 428, 1460

Calvi, R., Poggianti, B. M., Fasano, G., & Vulcani, B. 2012, Mon. Not. R. Astron. Soc., 419, L14

Cassata, P., Guzzo, L., Franceschini, A., Scoville, N., Capak, P., Ellis, R. S., Koekemoer, A., McCracken, H. J., Mobasher, B., Renzini, A., Ricciardelli, E., Scodeggio, M., Taniguchi, Y., & Thompson, D. 2007, Astrophys. J. Suppl. Ser., 172, 270

Cavanagh, M. K., Bekki, K., & Groves, B. A. 2023, Mon. Not. R. Astron. Soc., 520, 5885

Cerulo, P., Couch, W. J., Lidman, C., Demarco, R., Huertas-Company, M., Mei, S., Sánchez-Janssen, R., Barrientos, L. F., & Muñoz, R. 2017, Mon. Not. R. Astron. Soc., 472, 254

Chan, J. C. C., Wilson, G., Balogh, M., Rudnick, G., van der Burg, R. F. J., Muzzin, A., Webb, K. A., Biviano, A., Cerulo, P., Cooper, M. C., De Lucia, G., Demarco, R., Forrest, B., Jablonka, P., Lidman, C., McGee, S. L., Nantais, J., Old, L., Pintos-Castro, I., Poggianti, B., Reeves, A. M. M., Vulcani, B., Yee, H. K. C., & Zaritsky, D. 2021, Astrophys. J., 920, 32

Chiang, Y.-K., Overzier, R., & Gebhardt, K. 2013, Astrophys. J., 779, 127

Conselice, C. J. 2003, Astrophys. J. Suppl. Ser., 147, 1

—. 2014, Annu. Rev. Astron. Astrophys., 52, 291

Cooper, M. C., Newman, J. A., Madgwick, D. S., Gerke, B. F., Yan, R., & Davis, M. 2005, Astrophys. J., 634, 833

de Vaucouleurs, G. 1948, Annales d'Astrophysique, 11, 247

—. 1961, Astrophys. J. Suppl. Ser., 5, 233

Deeley, S., Drinkwater, M. J., Sweet, S. M., Bekki, K., Couch, W. J., Forbes, D. A., & Dolfi, A. 2021, Mon. Not. R. Astron. Soc., 508, 895

Deeley, S., Drinkwater, M. J., Sweet, S. M., Diaz, J., Bekki, K., Couch, W. J., Forbes, D. A., Bland-Hawthorn, J., Bryant, J. J., Croom, S., Cortese, L., Lawrence, J. S., Lorente, N., Medling, A. M., Owers, M., Richards, S. N., & van de Sande, J. 2020, Mon. Not. R. Astron. Soc., 498, 2372

Delahaye, A. G., Webb, T. M. A., Nantais, J., DeGroot, A., Wilson, G., Muzzin, A., Yee, H. K. C., Foltz, R., Noble, A. G., Demarco, R., Tudorica, A., Cooper, M. C., Lidman, C., Perlmutter, S., Hayden, B., Boone, K., & Surace, J. 2017, Astrophys. J., 843, 126

Djorgovski, S. & Davis, M. 1987, Astrophys. J., 313, 59

D'Onofrio, M., Marziani, P., & Buson, L. 2015, Frontiers in Astronomy and Space Sciences, 2, 4

Dressler, A. 1980, Astrophys. J., 236, 351

Dressler, A., Oemler, Augustus, J., Couch, W. J., Smail, I., Ellis, R. S., Barger, A., Butcher, H., Poggianti, B. M., & Sharples, R. M. 1997, Astrophys. J., 490, 577

Fang, J. J., Faber, S. M., Koo, D. C., Rodríguez-Puebla, A., Guo, Y., Barro, G., Behroozi, P., Brammer, G., Chen, Z., Dekel, A., Ferguson, H. C., Gawiser, E., Giavalisco, M., Kartaltepe, J., Kocevski, D. D., Koekemoer, A. M., McGrath, E. J., McIntosh, D., Newman, J. A., Pacifici, C., Pandya, V., Pérez-González, P. G., Primack, J. R., Salmon, B., Trump, J. R., Weiner, B., Willner, S. P., Acquaviva, V., Dahlen, T., Finkelstein, S. L., Finlator, K., Fontana, A., Galametz, A., Grogin, N. A., Gruetzbauch, R., Johnson, S., Mobasher, B., Papovich, C. J., Pforr, J., Salvato, M., Santini, P., van der Wel, A., Wiklind, T., & Wuyts, S. 2018, Astrophys. J., 858, 100

Fasano, G., Poggianti, B. M., Couch, W. J., Bettoni, D., Kjærgaard, P., & Moles, M. 2000, Astrophys. J., 542, 673

Ferreira, L., Conselice, C. J., Sazonova, E., Ferrari, F., Caruana, J., Tohill, C.-B., Lucatelli, G., Adams, N., Irodotou, D., Marshall, M. A., Roper, W. J., Lovell, C. C., Verma, A., Austin, D., Trussler, J., & Wilkins, S. M. 2023, Astrophys. J., 955, 94

Förster Schreiber, N. M. & Wuyts, S. 2020, Annu. Rev. Astron. Astrophys., 58, 661

Freeman, K. C. 1970, Astrophys. J., 160, 811

Gao, H., Ho, L. C., Barth, A. J., & Li, Z.-Y. 2018, Astrophys. J., 862, 100

Gillman, S., Tiley, A. L., Swinbank, A. M., Harrison, C. M., Smail, I., Dudzevičiūtė, U., Sharples, R. M., Cortese, L., Obreschkow, D., Bower, R. G., Theuns, T., Cirasuolo, M., Fisher, D. B., Glazebrook, K., Ibar, E., Mendel, J. T., & Sweet, S. M. 2020, Mon. Not. R. Astron. Soc., 492, 1492

Goto, T., Yamauchi, C., Fujita, Y., Okamura, S., Sekiguchi, M., Smail, I., Bernardi, M., & Gomez, P. L. 2003, Mon. Not. R. Astron. Soc., 346, 601

Grogin, N. A., Kocevski, D. D., Faber, S. M., Ferguson, H. C., Koekemoer, A. M., Riess, A. G., Acquaviva, V., Alexander, D. M., Almaini, O., Ashby, M. L. N., Barden, M., Bell, E. F., Bournaud, F., Brown, T. M., Caputi, K. I., Casertano, S., Cassata, P., Castellano, M., Challis, P., Chary, R.-R., Cheung, E., Cirasuolo, M., Conselice, C. J., Roshan Cooray, A., Croton, D. J., Daddi, E., Dahlen, T., Davé, R., de Mello, D. F., Dekel, A., Dickinson, M., Dolch, T., Donley, J. L., Dunlop, J. S., Dutton, A. A., Elbaz, D., Fazio, G. G., Filippenko, A. V., Finkelstein, S. L., Fontana, A., Gardner, J. P., Garnavich, P. M., Gawiser, E., Giavalisco, M., Grazian, A., Guo, Y., Hathi, N. P., Häussler, B., Hopkins, P. F., Huang, J.-S., Huang, K.-H., Jha, S. W., Kartaltepe, J. S., Kirshner, R. P., Koo, D. C., Lai, K., Lee, K.-S., Li, W., Lotz, J. M., Lucas, R. A., Madau, P., McCarthy, P. J., McGrath, E. J., McIntosh, D. H., McLure, R. J., Mobasher, B., Moustakas, L. A., Mozena, M., Nandra, K., Newman, J. A., Niemi, S.-M., Noeske, K. G., Papovich, C. J., Pentericci, L., Pope, A., Primack, J. R., Rajan, A., Ravindranath, S., Reddy, N. A., Renzini, A., Rix, H.-W., Robaina, A. R., Rodney, S. A., Rosario, D. J., Rosati, P., Salimbeni, S., Scarlata, C., Siana, B., Simard, L., Smidt, J., Somerville, R. S., Spinrad, H., Straughn, A. N., Strolger, L.-G., Telford, O., Teplitz, H. I., Trump, J. R., van der Wel, A., Villforth, C., Wechsler, R. H., Weiner, B. J., Wiklind, T., Wild, V., Wilson, G., Wuyts, S., Yan, H.-J., & Yun, M. S. 2011, Astrophys. J. Suppl. Ser., 197, 35

Gunn, J. E. & Gott, J. Richard, I. 1972, Astrophys. J., 176, 1

Harrison, C. M., Johnson, H. L., Swinbank, A. M., Stott, J. P., Bower, R. G., Smail, I., Tiley, A. L., Bunker, A. J., Cirasuolo, M., Sobral, D., Sharples, R. M., Best, P., Bureau, M., Jarvis, M. J., & Magdis, G. 2017, Mon. Not. R. Astron. Soc., 467, 1965

Holden, B. P., Illingworth, G. D., Franx, M., Blakeslee, J. P., Postman, M., Kelson, D. D., van der Wel, A., Demarco, R., Magee, D. K., Tran, K. V., Zirm, A., Ford, H., Rosati, P., & Homeier, N. 2007, Astrophys. J., 670, 190

Hubble, E. & Humason, M. L. 1931, Astrophys. J., 74, 43

Hubble, E. P. 1926, Astrophys. J., 64, 321

—. 1936, Realm of the Nebulae

Huertas-Company, M., Foex, G., Soucail, G., & Pelló, R. 2009, Astron. Astrophys., 505, 83

Huertas-Company, M., Kaviraj, S., Mei, S., O'Connell, R. W., Windhorst, R., Cohen, S. H., Hathi, . P., Koekemoer, A. M., Licitra, R., Raichoor, A., & Rutkowski, M. J. 2014, arXiv e-prints, arXiv:1406.1175

Huertas-Company, M., Rouan, D., Tasca, L., Soucail, G., & Le Fèvre, O. 2008, Astron. Astrophys., 478, 971

Joshi, G. D., Pillepich, A., Nelson, D., Marinacci, F., Springel, V., Rodriguez-Gomez, V., Vogelsberger, M., & Hernquist, L. 2020, Mon. Not. R. Astron. Soc., 496, 2673

Just, D. W., Zaritsky, D., Sand, D. J., Desai, V., & Rudnick, G. 2010, Astrophys. J., 711, 192

Kajisawa, M. & Yamada, T. 2006, Astrophys. J., 650, 12

Kartaltepe, J. S., Mozena, M., Kocevski, D., McIntosh, D. H., Lotz, J., Bell, E. F., Faber, S., Ferguson, H., Koo, D., Bassett, R., Bernyk, M., Blancato, K., Bournaud, F., Cassata, P., Castellano, M., Cheung, E., Conselice, C. J., Croton, D., Dahlen, T., de Mello, D. F., DeGroot, L., Donley, J., Guedes, J., Grogin, N., Hathi, N., Hilton, M., Hollon, B., Koekemoer, A., Liu, N., Lucas, R. A., Martig, M., McGrath, E., McPartland, C., Mobasher, B., Morlock, A., O'Leary, E., Peth, M., Pforr, J., Pillepich, A., Rosario, D., Soto, E., Straughn, A., Telford, O., Sunnquist, B., Trump, J., Weiner, B., Wuyts, S., Inami, H., Kassin, S., Lani, C., Poole, G. B., & Rizer, Z. 2015, Astrophys. J. Suppl. Ser., 221, 11

Kauffmann, G., Heckman, T. M., White, S. D. M., Charlot, S., Tremonti, C., Peng, E. W., Seibert, M., Brinkmann, J., Nichol, R. C., SubbaRao, M., & York, D. 2003, Mon. Not. R. Astron. Soc., 341, 54

Kauffmann, G., White, S. D. M., Heckman, T. M., Ménard, B., Brinchmann, J., Charlot, S., Tremonti, C., & Brinkmann, J. 2004, Mon. Not. R. Astron. Soc., 353, 713

Kawinwanichakij, L., Papovich, C., Quadri, R. F., Glazebrook, K., Kacprzak, G. G., Allen, R. J., Bell, E. F., Croton, D. J., Dekel, A., Ferguson, H. C., Forrest, B., Grogin, N. A., Guo, Y., Kocevski, D. D., Koekemoer, A. M., Labbé, I., Lucas, R. A., Nanayakkara, T., Spitler, L. R., Straatman, C. M. S., Tran, K.-V. H., Tomczak, A., & van Dokkum, P. 2017, Astrophys. J., 847, 134

Koekemoer, A. M., Faber, S. M., Ferguson, H. C., Grogin, N. A., Kocevski, D. D., Koo, D. C., Lai, K., Lotz, J. M., Lucas, R. A., McGrath, E. J., Ogaz, S., Rajan, A., Riess, A. G., Rodney, S. A., Strolger, L., Casertano, S., Castellano, M., Dahlen, T., Dickinson, M., Dolch, T., Fontana, A., Giavalisco, M., Grazian, A., Guo, Y., Hathi, N. P., Huang, K.-H., van der Wel, A., Yan, H.-J., Acquaviva, V., Alexander, D. M., Almaini, O., Ashby, M. L. N., Barden, M., Bell, E. F., Bournaud, F., Brown, T. M., Caputi, K. I., Cassata, P., Challis, P. J., Chary, R.-R., Cheung, E., Cirasuolo, M., Conselice, C. J., Roshan Cooray, A., Croton, D. J., Daddi, E., Davé, R., de Mello, D. F., de Ravel, L., Dekel, A., Donley, J. L., Dunlop, J. S., Dutton, A. A., Elbaz,

D., Fazio, G. G., Filippenko, A. V., Finkelstein, S. L., Frazer, C., Gardner, J. P., Garnavich, P. M., Gawiser, E., Gruetzbauch, R., Hartley, W. G., Häussler, B., Herrington, J., Hopkins, P. F., Huang, J.-S., Jha, S. W., Johnson, A., Kartaltepe, J. S., Khostovan, A. A., Kirshner, R. P., Lani, C., Lee, K.-S., Li, W., Madau, P., McCarthy, P. J., McIntosh, D. H., McLure, R. J., McPartland, C., Mobasher, B., Moreira, H., Mortlock, A., Moustakas, L. A., Mozena, M., Nandra, K., Newman, J. A., Nielsen, J. L., Niemi, S., Noeske, K. G., Papovich, C. J., Pentericci, L., Pope, A., Primack, J. R., Ravindranath, S., Reddy, N. A., Renzini, A., Rix, H.-W., Robaina, A. R., Rosario, D. J., Rosati, P., Salimbeni, S., Scarlata, C., Siana, B., Simard, L., Smidt, J., Snyder, D., Somerville, R. S., Spinrad, H., Straughn, A. N., Telford, O., Teplitz, H. I., Trump, J. R., Vargas, C., Villforth, C., Wagner, C. R., Wandro, P., Wechsler, R. H., Weiner, B. J., Wiklind, T., Wild, V., Wilson, G., Wuyts, S., & Yun, M. S. 2011, Astrophys. J. Suppl. Ser., 197, 36

Kriek, M., van Dokkum, P. G., Labbé, I., Franx, M., Illingworth, G. D., Marchesini, D., & Quadri, R. F. 2009, Astrophys. J., 700, 221

Larson, R. B., Tinsley, B. M., & Caldwell, C. N. 1980, Astrophys. J., 237, 692

Lidman, C., Suherli, J., Muzzin, A., Wilson, G., Demarco, R., Brough, S., Rettura, A., Cox, J., DeGroot, A., Yee, H. K. C., Gilbank, D., Hoekstra, H., Balogh, M., Ellingson, E., Hicks, A., Nantais, J., Noble, A., Lacy, M., Surace, J., & Webb, T. 2012, Mon. Not. R. Astron. Soc., 427, 550

Lin, L., Cooper, M. C., Jian, H.-Y., Koo, D. C., Patton, D. R., Yan, R., Willmer, C. N. A., Coil, A. L., Chiueh, T., Croton, D. J., Gerke, B. F., Lotz, J., Guhathakurta, P., & Newman, J. A. 2010, Astrophys. J., 718, 1158

Lotz, J. M., Primack, J., & Madau, P. 2004, Astron. J., 128, 163

Maiolino, R. & Mannucci, F. 2019, Astron. Astrophys. Rev., 27, 3

Matharu, J., Muzzin, A., Brammer, G. B., Nelson, E. J., Auger, M. W., Hewett, P. C., van der Burg, R., Balogh, M., Demarco, R., Marchesini, D., Noble, A. G., Rudnick, G., van der Wel, A., Wilson, G., & Yee, H. K. C. 2021, Astrophys. J., 923, 222

Matharu, J., Muzzin, A., Brammer, G. B., van der Burg, R. F. J., Auger, M. W., Hewett, P. C., van der Wel, A., van Dokkum, P., Balogh, M., Chan, J. C. C., Demarco, R., Marchesini, D., Nelson, E. J., Noble, A., Wilson, G., & Yee, H. K. C. 2019, Mon. Not. R. Astron. Soc., 484, 595

McGee, S. L., Bower, R. G., & Balogh, M. L. 2014, Mon. Not. R. Astron. Soc., 442, L105

McLeod, D. J., McLure, R. J., Dunlop, J. S., Cullen, F., Carnall, A. C., & Duncan, K. 2021, Mon. Not. R. Astron. Soc., 503, 4413

Mei, S., Hatch, N. A., Amodeo, S., Afanasiev, A. V., De Breuck, C., Stern, D., Cooke, E. A., Gonzalez, A. H., Noirot, G., Rettura, A., Seymour, N., Stanford, S. A., Vernet, J., & Wylezalek, D. 2023, Astron. Astrophys., 670, A58

Mei, S., Stanford, S. A., Holden, B. P., Raichoor, A., Postman, M., Nakata, F., Finoguenov, A., Ford, H. C., Illingworth, G. D., Kodama, T., Rosati, P., Tanaka, M., Huertas-Company, M., Rettura, A., Shankar, F., Carrasco, E. R., Demarco, R., Eisenhardt, P., Jee, M. J., Koyama, Y., & White, R. L. 2012, Astrophys. J., 754, 141

Melnick, J. & Sargent, W. L. W. 1977, Astrophys. J., 215, 401

Mihos, J. C. & Hernquist, L. 1994, Astrophys. J. Lett., 431, L9

Momcheva, I. G., Brammer, G. B., van Dokkum, P. G., Skelton, R. E., Whitaker, K. E., Nelson, E. J., Fumagalli, M., Maseda, M. V., Leja, J., Franx, M., Rix, H.-W., Bezanson, R., Da Cunha, E., Dickey, C., Förster Schreiber, N. M., Illingworth, G., Kriek, M., Labbé, I., Ulf Lange, J., Lundgren, B. F., Magee, D., Marchesini, D., Oesch, P., Pacifici, C., Patel, S. G., Price, S., Tal, T., Wake, D. A., van der Wel, A., & Wuyts, S. 2016, Astrophys. J. Suppl. Ser., 225, 27

Moore, B., Katz, N., Lake, G., Dressler, A., & Oemler, A. 1996, Nature, 379, 613

Moran, S. M., Ellis, R. S., Treu, T., Smith, G. P., Rich, R. M., & Smail, I. 2007, Astrophys. J., 671, 1503

Morishita, T., Ichikawa, T., & Kajisawa, M. 2014, Astrophys. J., 785, 18

Mortlock, A., Conselice, C. J., Hartley, W. G., Duncan, K., Lani, C., Ownsworth, J. R., Almaini, O., Wel, A. v. d., Huang, K.-H., Ashby, M. L. N., Willner, S. P., Fontana, A., Dekel, A., Koekemoer, A. M., Ferguson, H. C., Faber, S. M., Grogin, N. A., & Kocevski, D. D. 2015, Mon. Not. R. Astron. Soc., 447, 2

Mortlock, A., Conselice, C. J., Hartley, W. G., Ownsworth, J. R., Lani, C., Bluck, A. F. L., Almaini, O., Duncan, K., van der Wel, A., Koekemoer, A. M., Dekel, A., Davé, R., Ferguson, H. C., de Mello, D. F., Newman, J. A., Faber, S. M., Grogin, N. A., Kocevski, D. D., & Lai, K. 2013, Mon. Not. R. Astron. Soc., 433, 1185

Muldrew, S. I., Hatch, N. A., & Cooke, E. A. 2018, Mon. Not. R. Astron. Soc., 473, 2335

Muzzin, A., Wilson, G., Demarco, R., Lidman, C., Nantais, J., Hoekstra, H., Yee, H. K. C., & Rettura, A. 2013, Astrophys. J., 767, 39

Muzzin, A., Wilson, G., Yee, H. K. C., Gilbank, D., Hoekstra, H., Demarco, R., Balogh, M., van Dokkum, P., Franx, M., Ellingson, E., Hicks, A., Nantais, J., Noble, A., Lacy, M., Lidman, C., Rettura, A., Surace, J., & Webb, T. 2012, Astrophys. J., 746, 188

Muzzin, A., Wilson, G., Yee, H. K. C., Hoekstra, H., Gilbank, D., Surace, J., Lacy, M., Blindert, K., Majumdar, S., Demarco, R., Gardner, J. P., Gladders, M., & Lonsdale, C. 2009, Astrophys. J., 698, 1934

Nantais, J., Wilson, G., Muzzin, A., Old, L. J., Demarco, R., Cerulo, P., Balogh, M., Rudnick, G., Chan, J., Cooper, M. C., Forrest, B., Hayden, B., Lidman, C., Noble, A., Perlmutter, S., Rhea, C., Surace, J., van der Burg, R., & van Kampen, E. 2020, Mon. Not. R. Astron. Soc., 499, 3061

Nantais, J. B., Flores, H., Demarco, R., Lidman, C., Rosati, P., & Jee, M. J. 2013, Astron. Astrophys., 555, A5

Nantais, J. B., Muzzin, A., van der Burg, R. F. J., Wilson, G., Lidman, C., Foltz, R., DeGroot, A., Noble, A., Cooper, M. C., & Demarco, R. 2017, Mon. Not. R. Astron. Soc., 465, L104

Nantais, J. B., van der Burg, R. F. J., Lidman, C., Demarco, R., Noble, A., Wilson, G., Muzzin, A., Foltz, R., DeGroot, A., & Cooper, M. C. 2016, Astron. Astrophys., 592, A161

Overzier, R. A. 2016, Astron. Astrophys. Rev., 24, 14

Peng, C. Y., Ho, L. C., Impey, C. D., & Rix, H.-W. 2002, Astron. J., 124, 266

—. 2010a, Astron. J., 139, 2097

Peng, Y.-j., Lilly, S. J., Kovač, K., Bolzonella, M., Pozzetti, L., Renzini, A., Zamorani, G., Ilbert, O., Knobel, C., Iovino, A., Maier, C., Cucciati, O., Tasca, L., Carollo, C. M., Silverman, J., Kampczyk, P., de Ravel, L., Sanders, D., Scoville, N., Contini, T., Mainieri, V., Scodeggio, M., Kneib, J.-P., Le Fèvre, O., Bardelli, S., Bongiorno, A., Caputi, K., Coppa, G., de la Torre, S., Franzetti, P., Garilli, B., Lamareille, F., Le Borgne, J.-F., Le Brun, V., Mignoli, M., Perez Montero, E., Pello, R., Ricciardelli, E., Tanaka, M., Tresse, L., Vergani, D., Welikala, N., Zucca, E., Oesch, P., Abbas, U., Barnes, L., Bordoloi, R., Bottini, D., Cappi, A., Cassata, P., Cimatti, A., Fumana, M., Hasinger, G., Koekemoer, A., Leauthaud, A., Maccagni, D., Marinoni, C., McCracken, H., Memeo, P., Meneux, B., Nair, P., Porciani, C., Presotto, V., & Scaramella, R. 2010b, Astrophys. J., 721, 193

Pfeffer, J., Cavanagh, M. K., Bekki, K., Couch, W. J., Drinkwater, M. J., Forbes, D. A., & Koribalski, B. S. 2023, Mon. Not. R. Astron. Soc., 518, 5260

Poggianti, B. M., Desai, V., Finn, R., Bamford, S., De Lucia, G., Varela, J., Aragón-Salamanca, A., Halliday, C., Noll, S., Saglia, R., Zaritsky, D., Best, P., Clowe, D., Milvang-Jensen, B., Jablonka, P., Pelló, R., Rudnick, G., Simard, L., von der Linden, A., & White, S. 2008, Astrophys. J., 684, 888

Poggianti, B. M., Fasano, G., Bettoni, D., Cava, A., Dressler, A., Vanzella, E., Varela, J., Couch, W. J., D'Onofrio, M., Fritz, J., Kjaergaard, P., Moles, M., & Valentinuzzi, T. 2009, Astrophys. J. Lett., 697, L137

Postman, M., Franx, M., Cross, N. J. G., Holden, B., Ford, H. C., Illingworth, G. D., Goto, T., Demarco, R., Rosati, P., Blakeslee, J. P., Tran, K. V., Benítez, N., Clampin, M., Hartig, G. F., Homeier, N., Ardila, D. R., Bartko, F., Bouwens, R. J., Bradley, L. D., Broadhurst, T. J., Brown, R. A., Burrows, C. J., Cheng, E. S.,

Feldman, P. D., Golimowski, D. A., Gronwall, C., Infante, L., Kimble, R. A., Krist, J. E., Lesser, M. P., Martel, A. R., Mei, S., Menanteau, F., Meurer, G. R., Miley, G. K., Motta, V., Sirianni, M., Sparks, W. B., Tran, H. D., Tsvetanov, Z. I., White, R. L., & Zheng, W. 2005, Astrophys. J., 623, 721

Rawat, A., Wadadekar, Y., & De Mello, D. 2009, Astrophys. J., 695, 1315

Sandage, A. 1961, The Hubble Atlas of Galaxies

Sazonova, E., Alatalo, K., Lotz, J., Rowlands, K., Snyder, G. F., Boone, K., Brodwin, M., Hayden, B., Lanz, L., Perlmutter, S., & Rodriguez-Gomez, V. 2020, Astrophys. J., 899, 85

Sersic, J. L. 1968, Atlas de Galaxias Australes

Simard, L., Mendel, J. T., Patton, D. R., Ellison, S. L., & McConnachie, A. W. 2011, Astrophys. J. Suppl. Ser., 196, 11

Skelton, R. E., Whitaker, K. E., Momcheva, I. G., Brammer, G. B., van Dokkum, P. G., Labbé, I., Franx, M., van der Wel, A., Bezanson, R., Da Cunha, E., Fumagalli, M., Förster Schreiber, N., Kriek, M., Leja, J., Lundgren, B. F., Magee, D., Marchesini, D., Maseda, M. V., Nelson, E. J., Oesch, P., Pacifici, C., Patel, S. G., Price, S., Rix, H.-W., Tal, T., Wake, D. A., & Wuyts, S. 2014, Astrophys. J. Suppl. Ser., 214, 24

Smethurst, R. J., Masters, K. L., Simmons, B. D., Garland, I. L., Géron, T., Häußler, B., Kruk, S., Lintott, C. J., O'Ryan, D., & Walmsley, M. 2022, Mon. Not. R. Astron. Soc., 510, 4126

Strateva, I., Ivezić, Ž., Knapp, G. R., Narayanan, V. K., Strauss, M. A., Gunn, J. E., Lupton, R. H., Schlegel, D., Bahcall, N. A., Brinkmann, J., Brunner, R. J., Budavári, T., Csabai, I., Castander, F. J., Doi, M., Fukugita, M., Győry, Z., Hamabe, M., Hennessy, G., Ichikawa, T., Kunszt, P. Z., Lamb, D. Q., McKay, T. A., Okamura, S., Racusin, J., Sekiguchi, M., Schneider, D. P., Shimasaku, K., & York, D. 2001, Astron. J., 122, 1861

Strazzullo, V., Pannella, M., Mohr, J. J., Saro, A., Ashby, M. L. N., Bayliss, M. B., Canning, R. E. A., Floyd, B., Gonzalez, A. H., Khullar, G., Kim, K. J., McDonald, M., Reichardt, C. L., Sharon, K., & Somboonpanyakul, T. 2023, Astron. Astrophys., 669, A131

Tacconi, L. J., Genzel, R., & Sternberg, A. 2020, Annu. Rev. Astron. Astrophys., 58, 157

Tapia, T., Eliche-Moral, M. C., Aceves, H., Rodríguez-Pérez, C., Borlaff, A., & Querejeta, M. 2017, Astron. Astrophys., 604, A105

Tasca, L. A. M., Kneib, J. P., Iovino, A., Le Fèvre, O., Kovač, K., Bolzonella, M., Lilly, S. J., Abraham, R. G., Cassata, P., Cucciati, O., Guzzo, L., Tresse, L., Zamorani, G., Capak, P., Garilli, B., Scodeggio, M., Sheth, K., Zucca, E., Carollo, C. M., Contini, T., Mainieri, V., Renzini, A., Bardelli, S., Bongiorno, A., Caputi,

K., Coppa, G., de La Torre, S., de Ravel, L., Franzetti, P., Kampczyk, P., Knobel, C., Koekemoer, A. M., Lamareille, F., Le Borgne, J. F., Le Brun, V., Maier, C., Mignoli, M., Pello, R., Peng, Y., Perez Montero, E., Ricciardelli, E., Silverman, J. D., Vergani, D., Tanaka, M., Abbas, U., Bottini, D., Cappi, A., Cimatti, A., Ilbert, O., Leauthaud, A., Maccagni, D., Marinoni, C., McCracken, H. J., Memeo, P., Meneux, B., Oesch, P., Porciani, C., Pozzetti, L., Scaramella, R., & Scarlata, C. 2009, Astron. Astrophys., 503, 379

Taylor, E., Almaini, O., Merrifield, M., Maltby, D., Wild, V., Hartley, W. G., & Rowlands, K. 2023, Mon. Not. R. Astron. Soc., 522, 2297

Uzeirbegovic, E., Martin, G., & Kaviraj, S. 2022, Mon. Not. R. Astron. Soc., 510, 3849

van der Burg, R. F. J., Muzzin, A., Hoekstra, H., Lidman, C., Rettura, A., Wilson, G., Yee, H. K. C., Hildebrandt, H., Marchesini, D., Stefanon, M., Demarco, R., & Kuijken, K. 2013, Astron. Astrophys., 557, A15

van der Burg, R. F. J., Rudnick, G., Balogh, M. L., Muzzin, A., Lidman, C., Old, L. J., Shipley, H., Gilbank, D., McGee, S., Biviano, A., Cerulo, P., Chan, J. C. C., Cooper, M., De Lucia, G., Demarco, R., Forrest, B., Gwyn, S., Jablonka, P., Kukstas, E., Marchesini, D., Nantais, J., Noble, A., Pintos-Castro, I., Poggianti, B., Reeves, A. M. M., Stefanon, M., Vulcani, B., Webb, K., Wilson, G., Yee, H., & Zaritsky, D. 2020, Astron. Astrophys., 638, A112

van der Wel, A. 2008, Astrophys. J. Lett., 675, L13

van der Wel, A., Bell, E. F., Häussler, B., McGrath, E. J., Chang, Y.-Y., Guo, Y., McIntosh, D. H., Rix, H. W., Barden, M., Cheung, E., Faber, S. M., Ferguson, H. C., Galametz, A., Grogin, N. A., Hartley, W., Kartaltepe, J. S., Kocevski, D. D., Koekemoer, A. M., Lotz, J., Mozena, M., Peth, M. A., & Peng, C. Y. 2012, Astrophys. J. Suppl. Ser., 203, 24

van der Wel, A., Franx, M., van Dokkum, P. G., Skelton, R. E., Momcheva, I. G., Whitaker, K. E., Brammer, G. B., Bell, E. F., Rix, H. W., Wuyts, S., Ferguson, H. C., Holden, B. P., Barro, G., Koekemoer, A. M., Chang, Y.-Y., McGrath, E. J., Häussler, B., Dekel, A., Behroozi, P., Fumagalli, M., Leja, J., Lundgren, B. F., Maseda, M. V., Nelson, E. J., Wake, D. A., Patel, S. G., Labbé, I., Faber, S. M., Grogin, N. A., & Kocevski, D. D. 2014, Astrophys. J., 788, 28

van der Wel, A., Holden, B. P., Franx, M., Illingworth, G. D., Postman, M. P., Kelson, D. D., Labbé, I., Wuyts, S., Blakeslee, J. P., & Ford, H. C. 2007, Astrophys. J., 670, 206

Vulcani, B., Bamford, S. P., Häußler, B., Vika, M., Rojas, A., Agius, N. K., Baldry, I., Bauer, A. E., Brown, M. J. I., Driver, S., Graham, A. W., Kelvin, L. S., Liske, J., Loveday, J., Popescu, C. C., Robotham, A. S. G., & Tuffs, R. J. 2014, Mon. Not. R. Astron. Soc., 441, 1340

Wetzel, A. R., Tinker, J. L., Conroy, C., & van den Bosch, F. C. 2013, Mon. Not. R. Astron. Soc., 432, 336

Williams, R. J., Quadri, R. F., Franx, M., van Dokkum, P., & Labbé, I. 2009, Astrophys. J., 691, 1879

Wilson, G., Muzzin, A., Yee, H. K. C., Lacy, M., Surace, J., Gilbank, D., Blindert, K., Hoekstra, H., Majumdar, S., Demarco, R., Gardner, J. P., Gladders, M. D., & Lonsdale, C. 2009, Astrophys. J., 698, 1943

Wuyts, S., Förster Schreiber, N. M., Genzel, R., Guo, Y., Barro, G., Bell, E. F., Dekel, A., Faber, S. M., Ferguson, H. C., Giavalisco, M., Grogin, N. A., Hathi, N. P., Huang, K.-H., Kocevski, D. D., Koekemoer, A. M., Koo, D. C., Lotz, J., Lutz, D., McGrath, E., Newman, J. A., Rosario, D., Saintonge, A., Tacconi, L. J., Weiner, B. J., & van der Wel, A. 2012, Astrophys. J., 753, 114